Spring 2010

Foundry parameters for casting high-aluminum lightweight steel in complex shapes

Angella Marie Schulte

Department:

FOUNDRY PARAMETERS FOR CASTING HIGH-ALUMINUM LIGHTWEIGHT STEEL IN COMPLEX SHAPES

by

ANGELLA MARIE SCHULTE

A THESIS

Presented to the Faculty of the Graduate School of the

MISSOURI UNIVERSITY OF SCIENCE AND TECHNOLOGY

In Partial Fulfillment of the Requirements for the Degree

MASTER OF SCIENCE IN METALLURGICAL ENGINEERING

2010

Approved by:

David C. Van Aken, Co-Advisor
Von L. Richards, Co-Advisor
Kent D. Peaslee

PUBLICATION THESIS OPTION

This thesis consists of two articles submitted for publication as follows: each article is prepared according to the respective style of publication. Pages 8-38 have been accepted for publication in the Transactions of the American Foundry Society 2010, Volume 118 and are entitled "Phosphorus Mitigation in Cast Lightweight Fe-Mn-Al-C Steel." Pages 39-64 have been accepted for publication in the Transactions of the American Foundry Society 2010, Volume 118 and are entitled "Modeling for Improved Casting Quality of High-Aluminum Steels." The introduction and conclusion sections are completed in thesis format.

ABSTRACT

This work investigated the liquid metal treatment and molding practices for *Fe-30wt.%Mn-9wt.%Al-1wt.%Si-0.9wt.%C-0.5wt.%Mo* steel. The goal of this research was to determine the process conditions that would produce a tough *Fe-Mn-Al-C* alloy and the appropriate mold design to produce a defect-free P900 plate.

Notch toughness of age-hardenable *Fe-Mn-Al-C* alloys decreases as phosphorus increases. Thermodynamic calculations and experimental work show that additions of *Ca* followed by *Ce* can be used to mitigate the deleterious effects of phosphorus, and the addition of *Ar*-stirring can be used to decrease the number of harmful aluminum nitride inclusions. In the solution-treated and aged condition (Brinell hardness 317-330), the room temperature Charpy V-notch (CVN) impact energies increased from 33 J to 92 J as a result of ladle refinement using calcium wire, misch metal additions, and argon stirring with a lance. The addition of *Ar*-stirring decreased the number of inclusions by more than 90% when compared with the untreated heat.

Liquid *Fe-Mn-Al-C* alloys have casting characteristics significantly different from regular carbon steel; specifically, the high aluminum content promotes a strong tendency to re-oxidize and form surface films during mold filling. These melt properties promote the formation of oxide film laps and cold shuts in thin-walled castings. This research used MagmaSoft modeling software in conjunction with experiments to study the castability of *Fe-Mn-Al-C* steel P900 armor plates. The effects of superheat and venting procedures were evaluated for different molding techniques including bonded olivine sand molds tilted at both 0º and 15º from horizontal and pre-heated investment shell molds vertically oriented with a bottom-filled gating system. The best castings were produced in vertically oriented, bottom-filled, ceramic investment shell molds with a superheat of 300C° and poured directly from the furnace into a preheated investment shell at 800°C. Successful P900 castings were also obtained from the tilted bonded olivine sand molds when poured with a superheat above 300C°.

ACKNOWLEDGMENTS

This work was supported in part by the Leonard Wood Institute under the provisions of cooperative agreement W911NF-07-2-0062 with the Army Research Laboratory. I am also grateful to Waukesha Foundry, Inc. for providing the low-phosphorus *Fe-Mn-Al-C* alloy.

I would like to thank my advisors, David Van Aken and Von Richards, for their guidance and encouragement. I would also like to thank Kent Peaslee for serving as a committee member, and especially Simon Lekakh for his help with thermodynamic calculations and foundry experiments.

Forrest Huebner and Jacob Johnson deserve special recognition for helping me with mechanical and hands-on projects in the foundry and making work enjoyable during the summers. I would like to thank Jack Jones, Nathan Inskip, and Jimmie Taylor for all of their help in the machine shop and with repairs to foundry equipment. Other students who have helped me in various ways include Sam Buckholz and Michael Kuba.

Finally, I would like to thank my family for all of their support and their never-ending belief in my abilities during my educational journey.

TABLE OF CONTENTS

LIST OF ILLUSTRATIONS

LIST OF TABLES

SECTION

1. INTRODUCTION

1.1. PURPOSE

The purpose of this thesis is to develop the best molding and foundry practices to cast *Fe-30Mn-9Al-1Si-0.9C-0.5Mo* steel into complex shapes. Molding practices include the choice of sand or slurry material for the mold itself and the gating design to minimize inclusion formation. This study also examined steelmaking practice, metallurgical refinement of *Fe-30Mn-9Al-1Si-0.9C-0.5Mo* after steelmaking as well as melt transfer from furnace to ladle and ladle to mold.

1.2. BACKGROUND

Fe-Mn-Al-C steel is a lightweight alternative to low-alloy steel. The *Fe-Mn-Al-C* alloys evolved from Robert Hadfield's investigations of an *Fe-13Mn-1.2C* steel with a high toughness and excellent wear resistance.[1] All compositions reported in this thesis are given in weight percent. High aluminum alloys that are austenitic may be formulated by adding sufficient amounts of manganese and carbon. With additions of aluminum greater than 5.0% and of carbon greater than 0.3% these steels are age hardenable.[2] Howell et al. studied casting properties[3] and mechanical properties[4-6] and established a nominal composition of *Fe-30Mn-9Al-1Si-0.9C-0.5Mo* that met MIL-PRF-32669 requirements of cast military armor.[6] The low density of *Fe-30Mn-9Al-1Si-0.9C-0.5Mo* is a result of the high aluminum content. A linear reduction in density based upon lattice dilatation and atomic mass is a function of aluminum concentration for a range of manganese from 14-28%.[1] A silicon content of 1% was chosen for its combined effects on the liquidus and solidus temperatures and the addition of silicon has been shown to inhibit the formation of *β-Mn*. Liquidus and solidus temperatures decrease at a rate of 30C° per weight percent silicon added.[5] This amount of silicon does not promote excessive ferrite formation; and it inhibits the formation of *β-Mn*.

P900 refers to a class of appliqué armor with holes arranged in such a way that when the armor is hit by a projectile, the projectile is broken up due to the unequal load placed upon it.[7] These holes are designed at an oblique angle to further disrupt potential threats.[7] In the past P900 has been fabricated from wrought steel plates. The holes were either drilled or punched out of these wrought plates.[7] Punching and drilling are limited by plate thickness,[8] and the creation of P900 produces approximately 60% waste. The obvious answer to these problems is to cast P900.

The first P900 castings were produced using the lost foam process and an evaporative styrofoam pattern.[7] Casting P900 increased manufacturing yield and reduced the costs associated with machining.

P900 is a class 2 perforated armor[9] with a hardness requirement of 302-352 Brinell hardness number (BHN). The holes are of a staggered stacking sequence designed to produce a plate that is at most 50% by weight of a solid plate with the same dimensions. The holes are at an oblique angle of 25º to deflect and break up ballistic threats[10] (Figure 1.1).

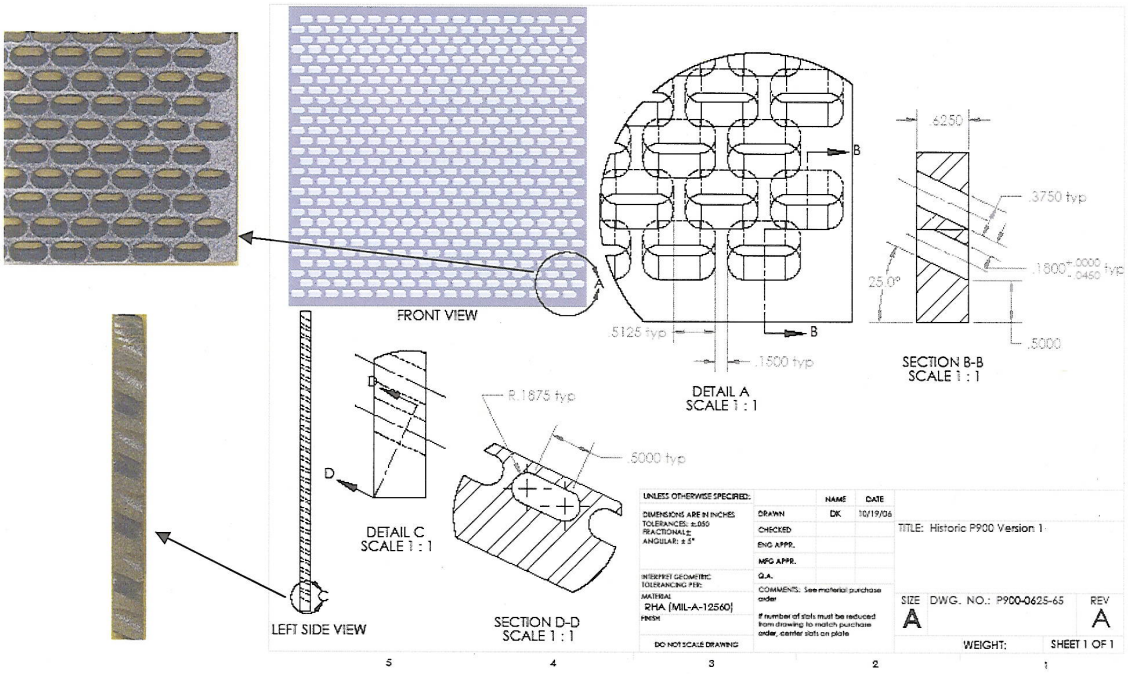

Figure 1.1. Image and 2-D specification drawing of cast P900 armor plate.

1.3. MOLD MATERIALS

Mold materials for *Fe-Mn-Al-C* castings are limited due to the high manganese content of the steel. It is standard practice to use olivine sand for high manganese steels, such as Hadfield steel, because it prevents defects such as rat-tails and buckles[11,12]. Olivine is basic[13] and does not react with manganese as silica sand does.[11,13-15] Another advantage of olivine sand over silica sand is that it does not undergo a volume change from a phase transformation. This abrupt

volume change causes the surface defects rat-tails and buckles.[14,15] The volume change can also cause sand to fall from the mold and cores while the metal is still liquid, resulting in sand inclusions.[14] Bonded sand, or no-bake, molding has several advantages. No-bake molds have excellent shake out characteristics because at steel pouring temperatures the resin bond in the sand is burned out in the areas surrounding the metal,[12] allowing easy removal of the casting from the mold. No-bake sand molds have a short curing time and are ready for use the same day.

Ceramic investment shell molds may also be used to produce P900. The investment molding process is capable of easily producing complex shapes. An investment shell is built of multiple layers consisting of a prime coat slurry, followed by an investment of slurry and coarse aggregate around a fugitive pattern that includes a feeding system.[16] The prime slurry contains a bonding agent that provides strength to the structure.[17] The prime coat also contains a finer refractory powder, is used at a higher viscosity, and is stuccoed with finer particles than back up coats.[17] This composition provides a smooth-surfaced mold capable of resisting metal penetration.[17] The back-up slurry is designed to provide strength and thickness with each successive coat. The coarse aggregate particles prevent run off of the slurry, prevent the next coat from cracking or pulling away, provide bonding between individual layers, and build thickness faster than just the back-up slurry alone.[17] The investment casting process is very versatile. Molds can be made for castings of any complexity, any castable alloy can be cast, and the products have close dimensional tolerances.[17] Limiting factors in the investment casting process are the difficulty in removing the shell without damaging the casting shell cracking, which leads to metal penetration may ruin the casting.

1.4. MOLD DESIGN

The second consideration before melting or casting is the mold design. The volumetric flow rate of the melt through a P900 mold must be high enough to prevent cold shuts. However, a high flow rate introduces the risk of turbulence, instabilities at the free surface of the liquid front, spraying effects, and subsequent reoxidation of the melt.[18] The high aluminum content of the steel studied here is susceptible to reoxidation, which can encourage oxidation laps and introduce high levels of nonmetallic inclusions.

If the P900 bonded sand mold were cast horizontally, the melt would initially fill the bottom of the mold cavity then gradually rise to the top.[19] This filling profile would trap defects along the entire top surface of the casting. There would be no control over the direction of flow of the melt in a horizontal casting orientation. The complex pattern of thin-webbed sections encourages many changes in liquid direction and velocity, which exposes more surface area of

the liquid to air, promoting oxide formation on the leading front as well as heat loss thereby creating the possibility of oxide laps and cold shuts.

If the P900 bonded sand mold were tilted up from the sprue, turbulence would be reduced in the runner, creating a more quiescent fill. Reduced turbulence helps prevent casting defects related to aluminum oxides[19] because the surface area of the melt exposed to air is reduced, which reduces the amount of reoxidation experienced. The risk of spraying also decreases[19] with reduced turbulence. Spraying, or jetting, is experienced when there is a reduction in area in a mold and the liquid metal enters a mold cavity at such a velocity that it is no longer a stream but individual droplets that are at risk of reoxidation. If the mold were to be tilted up from the sprue any defects related to filling would then be trapped along the back edge of the casting and a much smaller area would be affected as compared to the same mold filled horizontally.

Vertically casting P900 is easier with a ceramic investment shell mold than bonded sand mold. An investment shell is one piece whereas a bonded sand mold has a parting line. If the bonded sand mold is not assembled properly the mold may not completely contain the liquid metal. Van der Graaf et al.[18] studied mold filling with a bottom-filled thin plate to minimize changes in flow direction. Their experiments compared cast iron, aluminum, and water. Campbell[20] refers to a similar experiment by Nieswaag in which the Weber number was used to predict closely when turbulence would occur and therefore helped determine a critical velocity. Van der Graaf et al.[18] observed that filling with aluminum was more irregular than filling with cast iron. The Weber number, however, predicts that cast iron filling should be more irregular than aluminum.[18] The Weber number represents the ratio of inertial forces of the flow to surface tension[18] and is defined as

$$We = \frac{\rho L V^2}{\sigma} \tag{1}$$

where ρ is the density, L is the characteristic length parameter, V is the critical velocity, and σ is the surface tension.[20] Van der Graaf et al.[18] disagree with the use of the Weber number. Under the laminar-flow conditions of their study, surface tension dominated surface waves. These conditions are best described by the Ohnesorge number.[18] This number represents the ratio between viscosity and surface tension, which is related to the Reynolds number and the Weber number according to

$$Oh = \frac{We^{\frac{1}{2}}}{Re} \tag{2}$$

where *Oh* is the Ohnesorge number, *We* is the Weber number, and *Re* is the Reynolds number.[18] Van der Graaf et al. set the hydraulic diameter (D_h) as the length scale parameter (L) in the Reynolds number and set the length scale parameter in the Weber number as the wavelength (λ) of a surface instability. These substitutions result in

$$Oh = \frac{v\left(\frac{\lambda\rho}{\sigma}\right)^{\frac{1}{2}}}{D_h} \tag{3}$$

where v is the kinematic viscosity, ρ is the density, and σ is the surface tension.[18]

The critical range for the Weber number is 0.2-0.8. This range defines the maximum limit for flow conditions that are free from surface turbulence.[20] A critical velocity range was calculated for 4130 and *Fe-30Mn-9Al-1Si-0.9C-0.5Mo* for comparison. Once these velocities were determined they were used to calculate the critical Ohnesorge number range for the two alloys.

The surface tension (σ) was assumed to be 2 N/m for 4130 and *Fe-Mn-Al-C*. The density (ρ) of 4130 is 7.83 g/cm^3 and 6.7 g/cm^3 for *Fe-Mn-Al-C*. The characteristic length parameter (L) was set as 0.1800 in (0.4572 cm), which is the width of the webbed section in the P900 plate. The calculated critical velocities for 4130 and *Fe-Mn-Al-C* are shown in Table 1.1.

Equation 3 was used to calculate the critical Ohnesorge number range for 4130 and *Fe-Mn-Al-C*. The dynamic viscosity of 4130 and *Fe-Mn-Al-C* were estimated[21] as 0.05 Poise and 0.035 Poise, respectively. The dynamic viscosities were then divided by the density of the liquid 4130 and *Fe-Mn-Al-C* to get the kinematic viscosities (v) of $6.4\text{x}10^{-3}$ cm^2/s and $5.2\text{x}10^{-3}$ cm^2/s. The maximum λ was set as twice the thickness of the casting, 0.625 in (1.588 cm). The hydraulic diameter of the cavity (D_h) was the same as L from Eq. 1. The calculated Ohnesorge numbers are shown in Table 1.1. These results suggest that the *Fe-Mn-Al-C* alloy has a higher critical velocity and is less likely to experience turbulence. This is unlikely because *Fe-Mn-Al-C* is less viscous than 4130. The Weber number does not take into account viscosity while the Ohnesorge number does. The estimated Ohnesorge numbers are less than one, which suggests that surface turbulence is not a problem in the P900 mold under the parameters studied in this thesis.

Table 1.1. Calculated critical ranges of velocity and *Oh* for 4130 and *Fe-Mn-Al-C*.

Critical Velcocity Range (cm/s)		
We	**4130**	***Fe-Mn-Al-C***
0.2	10.6	11.4
0.8	21.1	22.9
Oh **(10^{-4})**		
4130		***Fe-Mn-Al-C***
11.0		8.3

1.5. FILLING

A third consideration before melting or casting is to determine how the mold will fill. This section focuses on defects that are pattern and alloy specific. *Fe-Mn-Al-C* is inherently more difficult to cast than most steels because it is subject to reoxidation. P900 itself is difficult to fill due to its many thin sections, T-junctions, and the direction and velocity changes that occur as the metal flows into the mold.

Fe-Mn-Al-C is susceptible to oxidation laps due to the high oxidation potential of aluminum. Oxidation laps form when metal streams fail to fuse due to the presence of an oxide layer on the leading front of the liquid.[19,20] Oxidation lap defects are commonly observed in castings that have been filled slowly.[20] At high flow rates, a high local velocity direction change occurs at intersections in the mold. The melt jets and splashes, causing air entrainment and creating oxide laps.[20] Slower liquid flow rates, or bigger gating section sizes, reduce local velocity changes in the direction. As a result, the oxidation products are not mixed in, but pushed ahead of the melt. Slower melt flow rates prevent excessive oxidation and inclusion entrapment.[20]

P900 is at risk of forming cold shuts due to the thin-webbed sections and the complicated fluid flow pattern these sections create. Cold shuts are discontinuities that form due to imperfect fusion where two streams of metal have converged.[22,23] They are characterized by rounded seams that may exist only on the surface or may continue through the thickness of the casting.[22,23] They form due to one or a combination of the following:[22,23] insufficient fluidity, slow or interrupted pouring, and insufficient venting. The volumetric flow rate of the liquid metal during filling is critical for preventing cold shuts.

One way to prevent cold shuts is to increase fluidity, which is directly related to superheat. Superheat also affects grain size and causes burn-on. Raising the pouring temperature can adversely increase grain size. Low pouring temperatures expand the region of equiaxed

grains and promote fine grain size in a casting.[24,25] The risk of the surface burn-on defect is increased with increasing superheat. Burn-on is a casting defect that occurs when liquid metal fills the voids in the sand mold or core causing sand to adhere to the casting surface.[26] Burn-on is severe enough that the casting surface must be blasted or cleaned by abrasive grinding.[26,27]

Cold shuts and oxidation laps severely weaken the casting. During ballistic testing these defects may cause far-field cracking, which reduces the multi-hit capability of P900 armor.

The section size, pouring rate, and fluidity of the alloy affect the ability to fill a mold completely and produce a sound casting.[24] The section size of a casting determines the pouring rate and fluidity needed to produce a sound casting. A complex and relatively thin mold, such as P900, requires higher fluidity and higher pouring rates than a solid plate mold of the same dimensions. If a pouring rate is too slow then the mold will not have enough time to fill before the melt begins to solidify and cold shuts form or the casting is incompletely filled. If there is not enough fluidity then the melt will be too viscous to completely fill thin or complex sections.

Insufficient or improper venting can cause high pressure areas in a mold and can lead to the formation of cold shut defects.[22,23] Venting allows gases to escape, which lowers the air pressure in the mold and allows a more controlled and quiescent fill.

1.6. MELTING, MELT HANDLING, AND MELT TREATMENT

The high aluminum content (9%) of *Fe-Mn-Al-C* renders the alloy prone to reoxidation. During melting, a cover flow of argon is used to prevent oxidation.[5] Melt transfer from furnace to ladle, then from ladle to mold, puts the melt at high risk for reoxidation. To avoid reoxidation-related defects, the melt should not be held for too long in the ladle, and a short, smooth pouring stream should be maintained to avoid splashing or a ragged stream.[25] Oxidation-related defects can be exacerbated by excessive additions of strong deoxidants[25] which is the natural state of *Fe-Mn-Al-C* with 9%Al. A high inclusion density has a detrimental effect on Charpy V-notch (CVN) impact toughness.[10,28-30]

There are three inclusion characteristics that influence toughness: inclusion volume fraction, inclusion spacing, and the resistance of the inclusions to void nucleation.[29,30] The particles that first nucleate voids are referred to as primary particles. In steels, primary particles can be sulfides, oxides, or nitrides.[29,30] In *Fe-Mn-Al-C*, aluminum nitride particles are most detrimental to CVN impact toughness.[10] When some sulfur is present in *Fe-Mn-Al-C*, manganese sulfide nucleates around the cuboidal aluminum nitride particles.[10] These complex inclusions are believed to be less detrimental to impact toughness than the aluminum nitride inclusions alone.[10]

CVN impact toughness is also affected by phosphorus content. The fracture mode of *Fe-Mn-Al-C* changes from a ductile fracture mode of microvoid coalescence to a brittle cleavage fracture with increasing phosphorus content.[3] Phosphorus segregation can also cause non hardening embrittlement in steels,[31,32] and phosphorus may segregate to the grain boundaries, which reduces grain boundary cohesion.[33-36] In the *Fe-30Mn-9Al-1Si-0.9C-0.5Mo* alloy the phosphorus is incorporated in the κ-carbide and the segregation of phosphorus to the grain boundaries produces preferential precipitation of κ-carbide and intergranular cleavage.[37]

Bangwen et al.[38] added rare earth metal (REM) additions to high-strength low-alloy (HSLA) steels in China and raised the toughness by 200%. Shul'te et al.[36] used additions of cerium in an attempt to mitigate the effects of phosphorus on austenitic high-manganese steel. For these reasons, this work studied additions of REM in *Fe-Mn-Al-C*.

1.7. SUMMARY

This research was performed to determine the best molding and steelmaking practices for casting clean, high-toughness *Fe-30Mn-9Al-1Si-0.9C-0.5Mo* steel. Thermodynamic modeling and experimental heats were analyzed to determine the best melting, melt handling, and liquid steel refining procedures for *Fe-Mn-Al-C*. Computational modeling using MAGMASOFT and experimental heats were used to determine the best mold design to minimize inclusion formation and macro defects, and to produce a P900 casting free of cold shuts and oxidation laps.

The goal of this research was to determine the best mold design and foundry procedures to produce a sound P900 plate cast from *Fe-30Mn-9Al-1Si-0.9C-0.5Mo* by minimizing casting-related defects, inclusions (oxides, nitrides, and sulfides), and trace pick-up (phosphorus). The combination of cold shuts, inclusions, and phosphorus is detrimental to the performance of *Fe-Mn-Al-C* P900 armor. Cold shuts affect the ability of P900 armor to absorb a blast because the defects cause through cracking. Inclusions can be detrimental to *Fe-Mn-Al-C* impact toughness, depending on their type, size, and distribution. Phosphorus adversely affects impact toughness by causing embrittlement in *Fe-Mn-Al-C*. Phosphorus mitigation was studied by sequences of additions including: *Ca* treatment, REM treatment, and an *Ar*-stirring method.

PAPER

1. Phosphorus Mitigation in Cast Lightweight *Fe-Mn-Al-C* Steel

Angella M. Schulte, Simon N. Lekakh, David C. Van Aken, Von L. Richards

Missouri University of Science and Technology

Department of Materials Science and Engineering

Rolla, Missouri 65409

Tel.: 573-341-4717

Email: dcva@mst.edu

Accepted for publication in the Transactions of the American Foundry Society 2010.

ABSTRACT

Notch toughness of age-hardenable *Fe-Mn-Al-C* alloys decreases as phosphorus increases. The study presented here shows by thermodynamic calculations and experimental work that additions of *Ca* and *Ce* can be used to mitigate the deleterious effects of phosphorus. *Ca* wire treatment, *Ce* treatment by misch metal addition, and *Ar*-stirring were tested for their effects on inclusion content, inclusion chemistry, and notch toughness in a nominal *Fe-30wt.%Mn-9wt.%Al-1wt.%Si-0.9wt.%C-0.5wt.%Mo* steel. Thermodynamic calculations were performed for melt treatment optimization. Five 80-lb heats were analyzed; the first was untreated, the second had a *Ca* addition, the third was treated with *Ca* and *Ce* additions. At various lengths *Ar*-stirring in the furnace was added to produce the fourth and fifth heats that were treated with *Ca* and *Ce*. Inclusion analysis showed that *P* combines with rare earth metals *Ce* and *La*, which are the major elements in misch metal, and that the population density of *AlN* inclusions directly affected the impact properties. In the solution-treated and aged condition (Brinell hardness 317-330), the room temperature Charpy V-notch (CVN) impact energies increased from 33 J to 92 J when comparing the untreated heat to the *Ca*, *Ce,* and *Ar*-treated heat. The heat with the highest concentration of *AlN* particles had a CVN impact energy of 19 J at -40° in the solution-treated and aged condition; and the heat with the lowest concentration of *AlN* had CVN impact energy of 38 J. The addition of *Ar*-stirring decreased the number of inclusions by more than 90% when compared with the untreated heat.

INTRODUCTION

Relative to low alloy-steels (such as 4130) the *Fe-Mn-Al-C* alloys containing 20-30% *Mn*, 7-12% *Al*, and 0.7-1.2% *C* have high specific strength under quasi-static tensile and high strain rate compression test conditions[1]. The addition of 7-12% *Al* lowers the density of steel by lattice dilation and by a reduction in mass. A duplex ferrite and austenite structure is typically observed at the higher *Al* contents, and a 16% reduction in density over conventional steels may be achieved by the addition of 12% *Al*. *Fe-Mn-Al-C* alloys age harden by precipitation of the κ-carbide[2], $(Fe,Mn)_3AlC$, when *Al* concentrations exceed 5% and *C* content is greater than 0.3%. In the alloy *Fe-30Mn-9Al-1Si-0.9C-0.5Mo*, a fully austenitic microstructure is achieved after a two-hour solution treatment above 950°C (1742ºF), and the density is 14.8% less than 4130. Peak

hardness is achieved by aging at 530°C (986ºF) for 30 hours. Hardness increases from 224 BHN to 372 BHN, tensile strength increases from 687 MPa to 1,065 MPa, and elongation to failure decreases from 44 to 8% by age hardening after solution treatment. The addition of 1% *Si* improves castability and ductility in peak aged materials by preventing the formation of the *β-Mn* phase[3]. Also, strength and notch toughness of precipitation-hardened *Fe-Mn-Al-C* alloys strongly depends on the *P* content[4]. Phosphorus promotes the formation of κ-carbide, increases hardness, and decreases the time to peak aging. Notch toughness is adversely affected by *P* by lowering the cleavage fracture stress of the κ-carbide. These two effects, enhanced κ-carbide precipitation in *P*-rich regions of the microstructure and cleavage fracture, promote intergranular fracture in castings because *P* segregates to the grain boundaries during solidification.

Phosphorus segregation during solidification and heat treatment has been studied experimentally in many types of steel. In 3.6*Ni* and 1.7*Cr* alloyed steel, *P* concentration at grain boundaries was nearly doubled during aging at 650°C (1202ºF)[5]. Grain boundary segregation of *P* was also reported[6] in the temperature range of 650-800°C (1202-1472ºF) for a commercial 17*Cr* and 12*Ni* austenitic steel. Solution treatment of *Fe-Mn-Al-C* steel requires cooling through this embrittlement temperature regime. Phosphorus segregation during cooling may help to explain the quench sensitivity of the notch toughness[4]. Phosphorus cannot be removed effectively during steelmaking in steels with high concentrations of *Mn* and *Al*. However, *P* has a moderate affinity to *Ca* and rare earth metals (REM) such as *Ce* and *La*. Thus, ladle refinement by the addition of *Ca* or misch metal, which contains predominately *Ce* and *La*, is a possible solution for decreasing *P* in the liquid and subsequently reducing the grain boundary segregation.

The objective of this research was the study of *P* mitigation in precipitation-hardened *Fe-Mn-Al-C* austenitic steel by additions of *Ca* and *Ce* during steelmaking.

Thermodynamic properties of REM and *Ca* phosphides were calculated here using published experimental data by Schlesinger[7]. *Ce* and *La* monophosphides have substantial negative Gibbs free energy values at elevated temperatures and could be stable during steelmaking, subsequent solidification, and heat treatment. Raghavan[8] published a *Ce-P-Fe* ternary phase diagram showing three intermediate *Ce-P* compounds: *CeP* (cubic, *NaCl* type), CeP_2 (monoclinic), and CeP_5 (monoclinic). This diagram also shoes three ternary compounds: $CeFe_2P_2$, $Ce_2Fe_{12}P_7$, and $CeFe_4P_{12}$. Work by Qin et al.[9] examined the behavior of *La* and *Ce* on grain boundaries in carbon-manganese steel and Ohta and Suito[10] have reported that the REMs tend strongly to segregate to austenite grain boundaries. Thus, at suitable REM content, the segregation of *P* at grain boundaries could be mitigated, leading to a significant increase in notch toughness.

PROCEDURES

PROCESS DESIGN

Refinement of reactions in *Fe-Mn-Al-C* alloys containing 20-30%*Mn*, 7-12%*Al*, 1%*Si*, and 0.7-1.2%*C* is quite different from that of previously studied steels. High *Mn* and *Al* contents should significantly influence the activity of dissolved impurities in the melt. Here, FactSage software with a comprehensive database was used to model the refining process and determine the appropriate sequence of *Ca* and REM additions to react with *P* in the melt. Minimization of the calculated Gibbs energy was used to predict the reaction products and final equilibrium conditions. The software's thermodynamic data set does not include the *Fe-30Mn-9Al-1Si-0.9C-0.5Mo* alloy. For the calculations presented here, an iron-based face centered cubic (FCC) database was used with elevated additions of *Mn*, *Al*, and *C*. The analysis also included sulfides, oxides, nitrides, and phosphides. Thermodynamic properties of *P*-REM compounds were added to the database using the work of Schlesinger[7]. Binary *Fe-Mn* and *Fe-Al* phase diagrams were calculated and compared to published phase diagrams to verify calculations. Segregation during solidification was calculated using a modified Scheil model, and the fraction of solid was incrementally removed and the remaining liquid containing the segregated alloy was allowed to solidify. Figure 1a shows an example of the Scheil model calculations for *P* segregation during solidification of *Fe-Mn-Al-C* steel with various *P* contents. A dramatic increase in segregation was obtained for a *P* content of 0.06%, but little segregation was observed below 0.01%. As shown in Figure 1b solid solubility of *P* in austenite at equilibrium with iron phosphide, Fe_2P, dramatically decreased as the temperature decreased. Thus, a promising approach to *P* mitigation is the addition of strong phosphide-forming elements, which would limit the solid solubility of *P* in the austenite.

Inclusion compositions in the base *Fe-Mn-Al-C* melt with 0.02%*S* and 0.05%*O* were estimated thermodynamically as preparation for the study of a refining reaction. Thermodynamic calculations predict the existence of Al_2O_3 and *MnS* phases, whereas *Al* can also form stable *AlN*. The refining reactions with increased *Ca* additions were then thermodynamically modeled and three reactions became possible. *Ca* in low concentrations was found to be very effective in gettering sulfur and forming *CaS*. Alumina was modified to form solid calcium aluminate, but began to form liquid calcium aluminate with additions of more than 0.05% *Ca* (see Figure 2). If both *S* and *O* fully react with *Ca*, then it may be possible to form the Ca_3P_2 phase with an addition of excess *Ca* (see Figure 3). Unfortunately, the stability of this phase in the melt is

limited by solidification temperatures and high carbon activity, which promotes the reaction of excess, or free, *Ca* with *C* to form CaC_2 at lower temperatures (see Figure 4). Thus, *Ca* alone cannot be used to mitigate *P*, but would serve as an important component of the refining process to remove *S*.

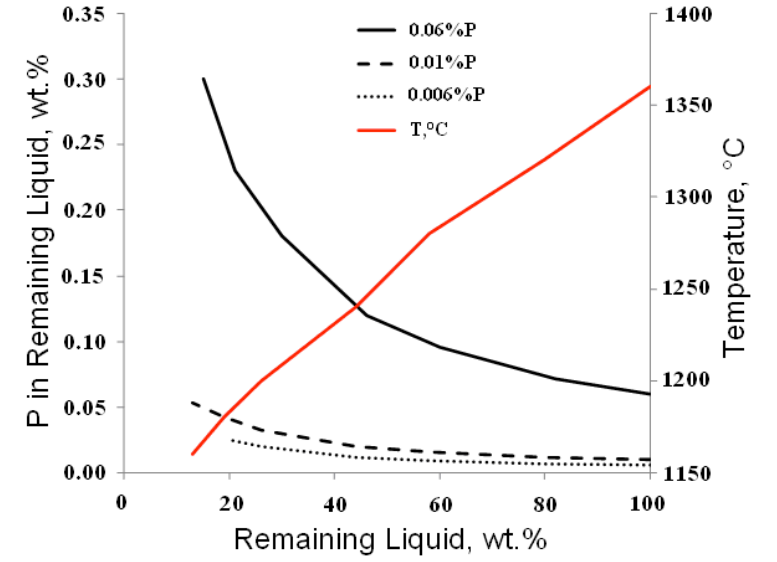

(a)

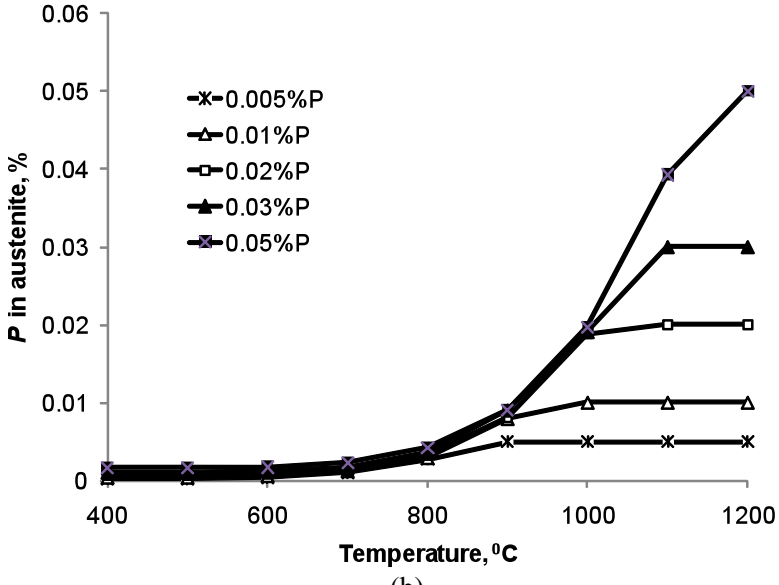

(b)

Figure 1. *P* segregation (Scheil model) during solidification (a) and equilibrium solubility of *P* in austenite (b) of *Fe-Mn-Al-C* steel.

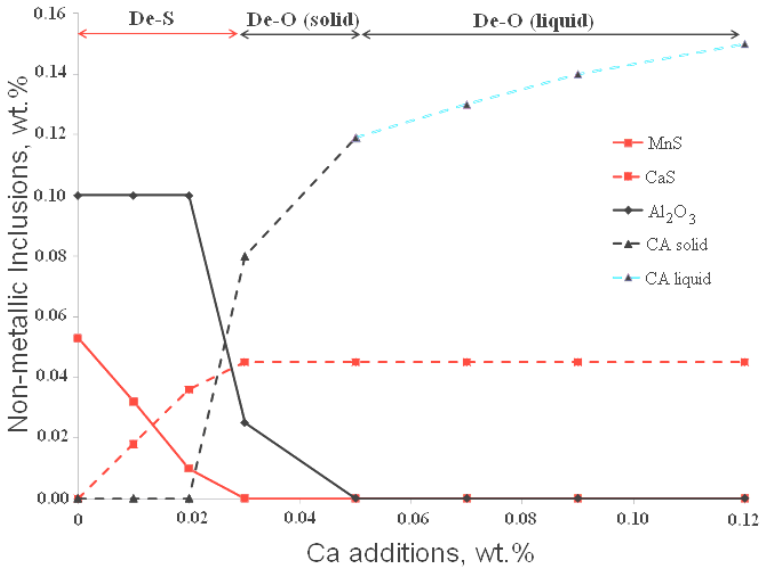

Figure 2. Calculated sequence of *Ca*, *S*, and *O* reactions in *Fe-Mn-Al-C* steel.

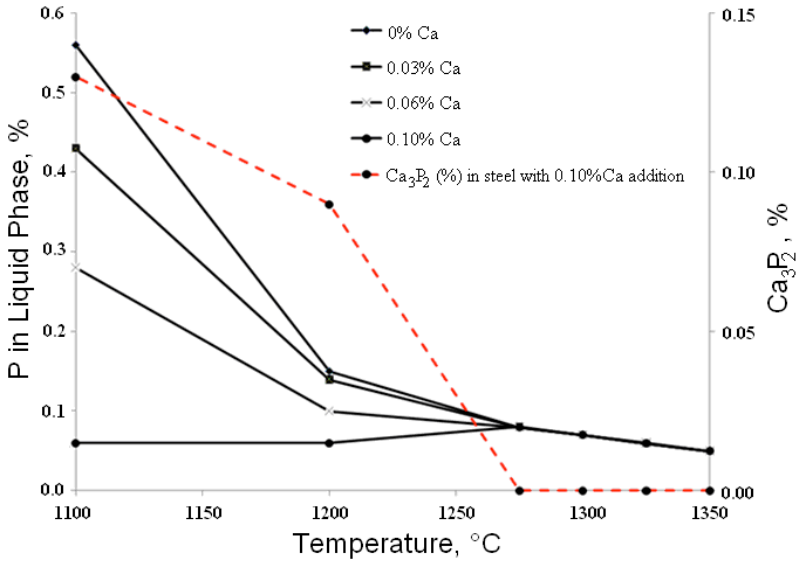

Figure 3. Calculated sequence of *Ca* and *P* reactions in *Fe-Mn-Al-C* steel.

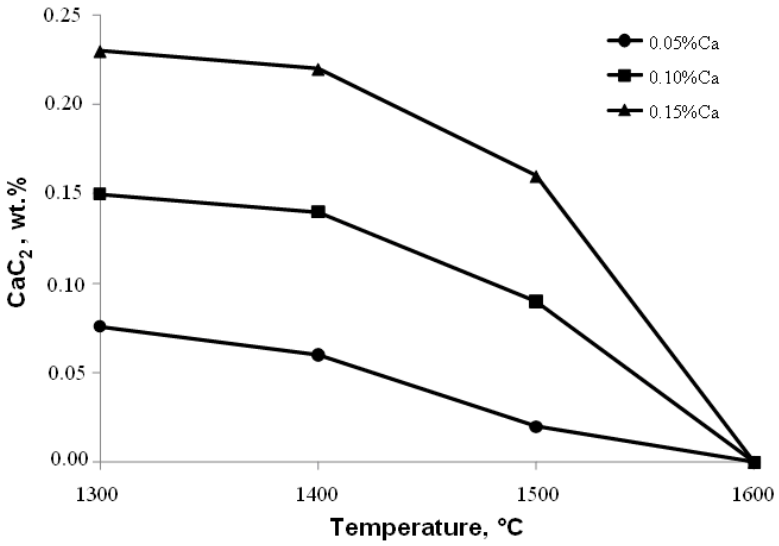

Figure 4. Calculated sequence of *Ca* and *C* reactions in *Fe-Mn-Al-C* steel.

Ce additions to a melt with 0.02%*S* and 0.05%*O* were modeled next. The sequence of reactions for the *Ce* addition followed a trend similar to that of *Ca*. *Ce* reacted first with *S* and, as *Ce* concentration increased, alumina was displaced by cerium oxide (see Figure 5). Thermodynamic data showed that REM phosphides are less stable than sulfides. Theoretically a *Ca* treatment would fully react with *S* and *O*, which would make *Ce* available to react with *P* (see Figure 6).

During melt solidification, the liquid phase becomes saturated with *P* due to its limited solid solubility in austenite. Thermodynamic properties of *P*-REM compounds determined by Schlesinger[7] were added to the thermodynamic software database. The reaction of free *Ce* with *P* was calculated at solidification temperatures (see Figure 7) and showed that *P*-REM compounds did not form in the melt above the liquidus temperature. Decreasing the temperature and increasing the *P* composition of the remaining melt promoted the formation of *P*-containing compounds. Both *Ce-P* and *Ce-O-P* phases would have been possible. The reaction with *Ce* decreased the free *P* in the remaining liquid phase as solidification progressed (Figure 7a). The optimum addition of *Ce* depends upon the initial *P* content in the melt, as shown in Figure 7b.

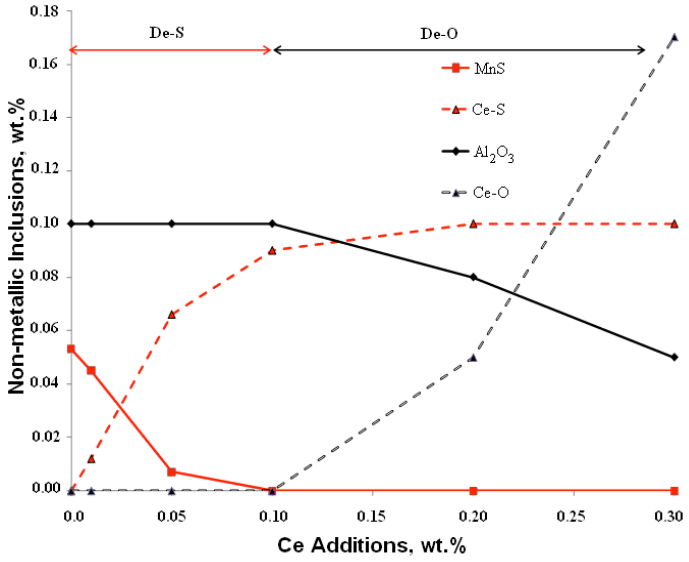

Figure 5. Calculated sequence of *Ce*, *S*, and *O* reactions in *Fe-Mn-Al-C* steel.

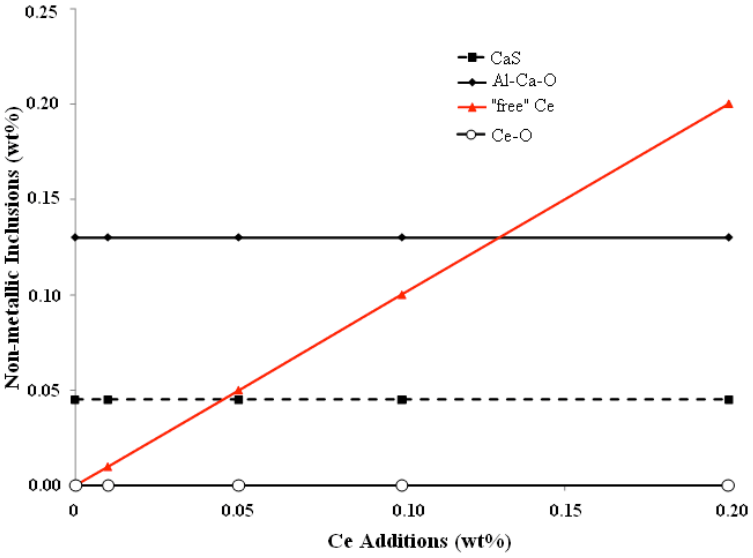

Figure 6. Calculated sequence of *Ca*- followed by *Ce*-addition in *Fe-Mn-Al-C* steel.

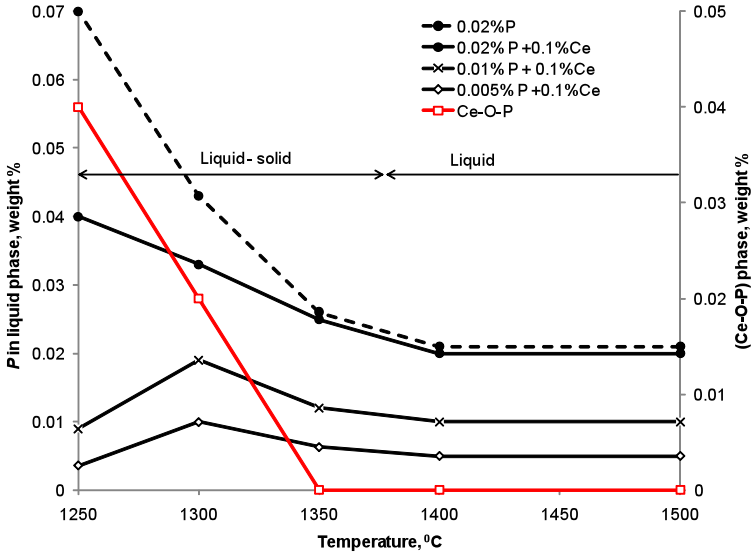

(a)

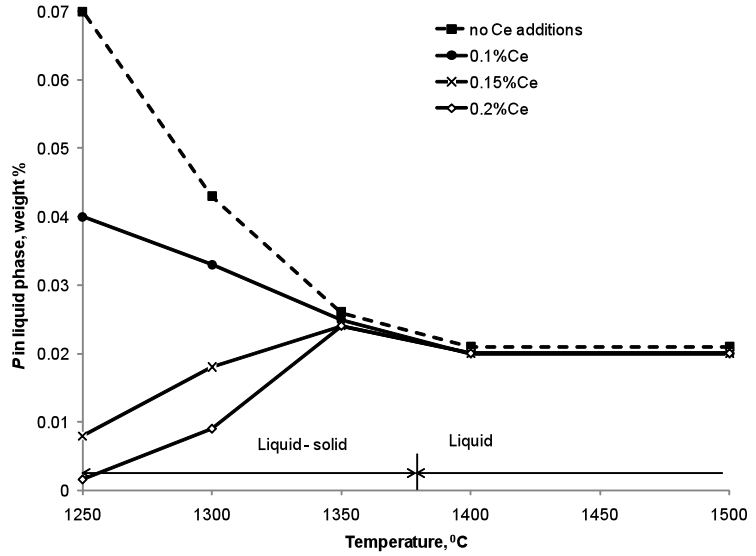

(b)

Figure 7. Calculated saturation of liquid phase by *P* during solidification of *Fe-Mn-Al* steel treated by *Ce*: (a) 0.1% "free" *Ce* in the melt with various levels of *P*; (b) various levels of free *Ce* in the melt with 0.02%*P*.

Finally, thermodynamic calculations were performed to optimize free *Ce* concentrations in *Fe-Mn-Al-C* with various *P* contents (0.01, 0.02, and 0.05wt.%*P*) in equilibrium with austenite (see Figure 8-10). Below 800°C (1472ºF), austenitic steel with 0.01wt%*P* began to form Fe_3P and the large amount of *P* begins precipitating out at 1000°C (1832ºF) in steel with 0.02 and

0.05wt%*P*. *Ce* additions to the melt immediately reacted to form *CeP* after completion of the reactions with *S* on *O*. As the free *Ce* content increased, the amount of Fe_3P formed decreased. At a ratio of five *Ce* to one *P*, no iron phosphides formed, and the amount of *P* remaining in the austenite was less than 0.001wt%.

Floatation of high density REM containing inclusions is difficult due to the lower melt density of the *Fe-Mn-Al-C* (6.7 g/cm^3) as compared to low-alloy steels (7.8 g/cm^3). The high density of *Ce* inclusions, such as cerium oxide (7.65 g/cm^3), as compared to more common inclusions such as alumina (4.1 g/cm^3) also makes floatation by natural convection difficult. *Fe-Mn-Al-C* steels typically range from one to five microns in diameter. Floatation in the ladle during free convection of the melt was modeled for both REM and alumina inclusions with a five-micron diameter. The results show that floatation was very slow (see Figure 11). However, *Ar*-stirring with a submerged lance has the potential to remove inclusions with various densities in a short time. Based upon these modeling studies, *P* mitigation in the *Fe-Mn-Al-C* alloys may be achieved by the following refining sequence: (1) *Ca* treatment to lower *S* and *O* activity, (2) de-slagging to remove *Ca* products, (3) misch metal addition of 0.1-0.2%, and (4) *Ar*-stirring.

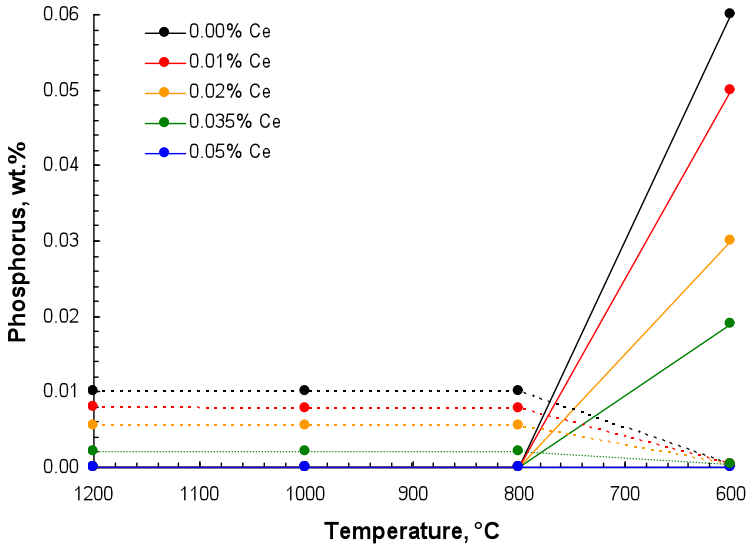

Figure 8. Thermodynamic predictions for a *Fe-Mn-Al-C* steel with an overall *P* content of 0.01wt%. The solid lines indicate the amount of *P* used to form the phosphide Fe_3P, and the dashed lines indicate the amount of *P* in the austenite. At 800°C (1472ºF) the *P* precipitated out of the austenite and forms Fe_3P.

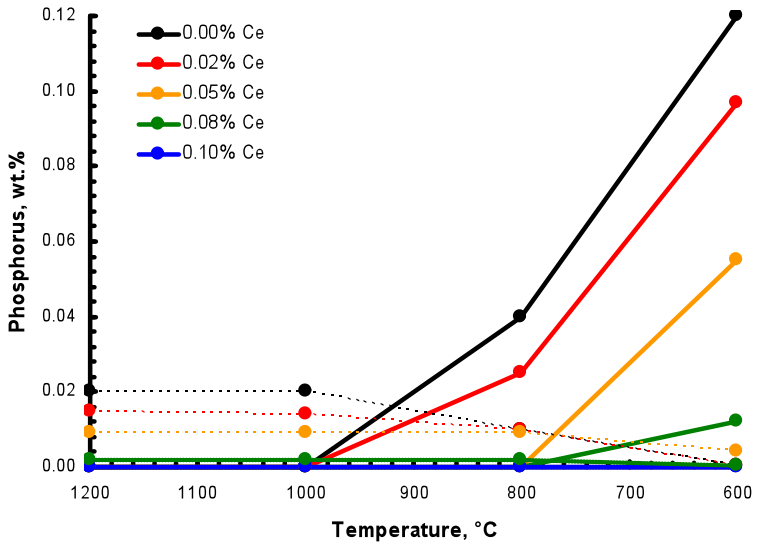

Figure 9. Thermodynamic predictions for a *Fe-Mn-Al-C* steel with an overall *P* content of 0.02wt%. The solid lines indicate the amount of *P* used to form the phosphide Fe_3P, and the dashed lines indicate the amount of *P* in the austenite. At 1000°C (1832ºF) *P* began to form Fe_3P at low concentrations of *Ce*, and at 800°C (1472ºF) the P precipitated out of the austenite at the higher concentrations of *Ce* (0.05 and 0.08wt%) at 0.02wt%*P*.

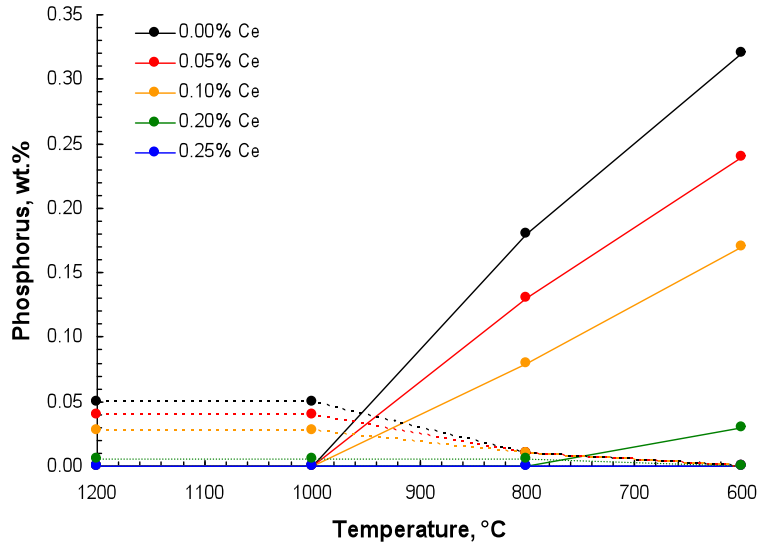

Figure 10. Thermodynamic predictions for a *Fe-Mn-Al-C* steel with an overall *P* content of 0.05wt%. The solid lines indicate the amount of *P* used to form the phosphide Fe_3P, and the dashed lines indicate the amount of *P* in the austenite. At 1000°C (1832ºF), *P* begins to form Fe_3P at most concentrations of *Ce*. At 800°C (1472ºF) the *P* precipitated out of the austenite at the higher concentrations of *Ce* (0.20wt%) at 0.05wt%*P*.

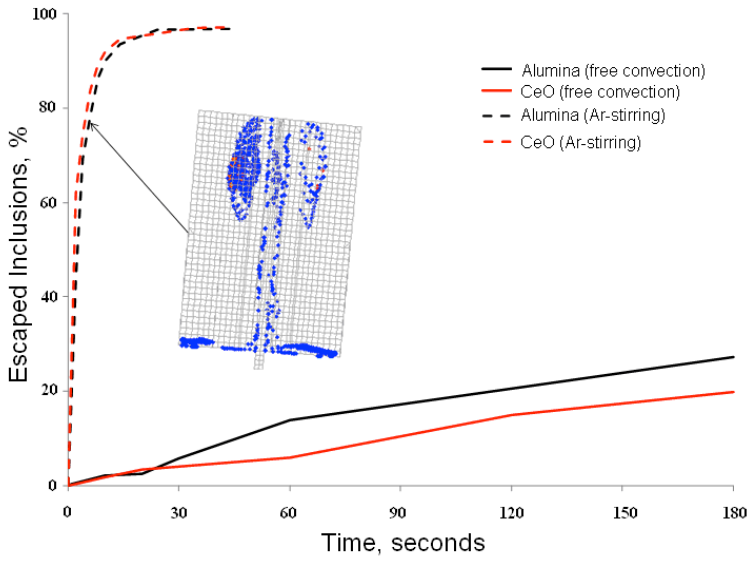

Figure 11. Floatation of inclusions (five microns) in the *Fe-Mn-Al-C* melt with free convection and in the *Ar*-stirred melt. The graphic represents a snapshot, at 60 seconds, of the inclusion distribution at the middle vertical section of the ladle resulting from *Ar*-stirring.

EXPERIMENTAL PROCEDURES

Alloys were melted in a high-frequency, 100-pound induction furnace under *Ar* gas cover flowing at a rate of 30 standard cubic feet per hour (scfh). High-purity induction iron, aluminum, and carbon were used in conjunction with additions of electrolytic manganese, ferrosilicon, and ferromolybdenum. The furnace was initially charged with aluminum, carbon, ferrosilicon, ferromolybdenum, and 30% of the induction iron. After the initial charge melted, the remainder of the induction iron was added to the melt. Electrolytic manganese was added in the furnace last to ensure maximum solubility in the alloy melt and to minimize losses by vaporization and slag formation. Melt stirring was limited to that provided by induction heating, natural convection, pouring from the furnace to the ladle, and casting, except in the case of the fourth and fifth heats. All heats were tapped from the furnace at 1650°C (3002ºF) and poured into five bonded olivine sand keel block molds (see Figure 12) with a top riser.

Four heats of a nominal *Fe-30Mn-9Al-0.9C-1Si-0.9C-0.5Mo* chemistry were cast. The first was a base heat, the second was treated with 0.15wt.%*Ca*, and the third was treated with 0.15wt.%*Ca*, and 0.2wt.%*Ce*. The fourth heat was treated with 0.15wt.%*Ca* and 0.2wt.%*Ce* then *Ar*-stirred in the furnace for 60 seconds at a flow rate of 12 scfh using a submerged lance with a porous plug (see Figure 13). Table 1 lists the heat chemistries as determined by inductive

coupled plasma spectrometry and wavelength dispersive spectrometry after dissolution of the steel in perchloric acid.

A fifth heat was cast in the nominal *Fe-30Mn-9Al-1Si-0.9C-0.5Mo* alloy and treated in the same manner as Heat 4. The procedure differed in terms of the time for *Ar*-stirring and the pouring technique. The melt was *Ar*-stirred for 30 seconds (at a flow rate of 12 scfh) in the furnace using a submerged lance with a porous plug. Heat 5 was *Ar*-stirred for half the time of Heat 4 to avoid over-exposure to the atmosphere during melt treatment. The heat was tapped from the furnace at 1650°C (3002ºF) and poured from a teapot-style ladle created from the standard lip-pour ladle inserts by inserting a ceramic dam. The melt was then *Ar*-stirred for 15 seconds before pouring five bonded olivine sand keel block molds. Table 1 shows the chemistry for Heat 5.

Charpy impact specimens were machined from each heat, and tests were performed at room temperature (as cast, solution treated, and aged) and at -40° for the age-hardened material only. All heat treatments were performed using chemically coated stainless steel bags to prevent decarburization and oxidation. Solution treating was performed on each heat for two hours at 1050°C (1922ºF), and the specimens were subsequently water quenched. Samples from each heat were aged in a molten salt bath for 20 hours at 530°C (986ºF), then water quenched. Fracture analysis was performed using scanning electron microscopy (SEM). An ASPEX PICA 1020 analytical SEM was used to quantitatively compare material cleanliness by examining inclusion chemistry, size distribution, and inclusion density.

Charpy impact specimens were machined from each heat, and tests were performed at room temperature (as cast, solution treated, and aged) and at -40° for the age-hardened material only. All heat treatments were performed using chemically coated stainless steel bags to prevent decarburization and oxidation. Solution treating was performed on each heat for two hours at 1050°C (1922ºF), and the specimens were subsequently water quenched. Samples from each heat were aged in a molten salt bath for 20 hours at 530°C (986ºF), then water quenched. Fracture analysis was performed using scanning electron microscopy (SEM). An ASPEX PICA 1020 analytical SEM was used to quantitatively compare material cleanliness by examining inclusion chemistry, size distribution, and inclusion density.

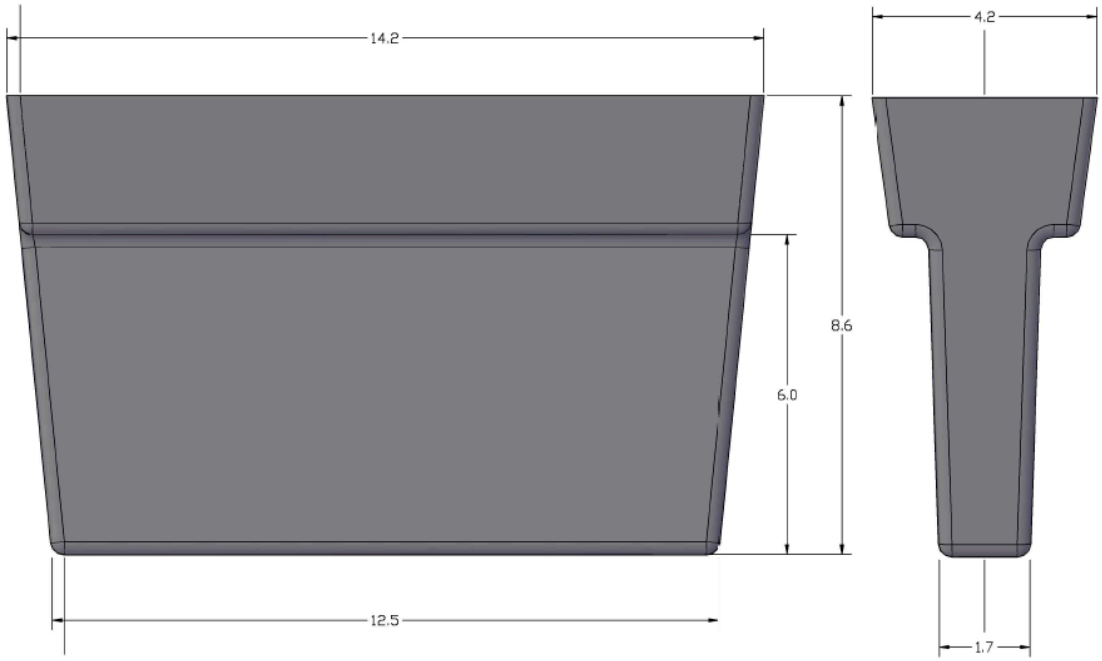

Figure 12. CAD drawing of keel block casting with dimensions given in centimeters. The riser was located at the middle of the top of the casting.

Figure 13. The *Ar* bubbling lance (a) used to help clean Heats 4 and 5. The lance (b) was submerged into the heat. The porous plug (c) was sufficient to produce visible bubbling throughout the submersion.

Table 1. Chemical analyses of cast heats in weight percent

Heat #	*Mn*	*Al*	*Si*	*C*	*Mo*	*P*	*S*	*Ce*	*La*	*Fe*
Heat 1	30.30	8.72	1.15	0.85	0.34	0.030	0.010	<0.01	<0.01	balance
Heat 2	30.11	8.86	0.94	0.92	0.33	0.030	<0.005	<0.01	<0.01	balance
Heat 3	30.12	8.64	0.86	0.95	0.34	0.025	<0.005	0.040	0.011	balance
Heat 4	30.30	8.76	1.02	0.94	0.38	0.030	<0.005	0.023	<0.01	balance
Heat 5	30.09	8.25	1.19	0.93	0.42	0.017	<0.005	<0.007	0.008	balance

RESULTS

Representative inclusions from each refining process are shown in Figure 14. Aluminum nitrides were found in each heat. In the base heat, *AlN* was found to be part of a complex inclusion consisting of an *AlN* core surrounded by *MnS*. Calcium treatment modified the *MnS* to a complex *Ca-Mn-S* inclusion. Many of the *Ce*- and *La*-bearing inclusions in Heat 3 (*Ca* and *Ce* treated) had elevated concentrations of *P*. Inclusion compositions from Heat 3 are shown in Figure 15. Table 2 shows the chemical analyses of the *Ce-Ca-P* and *Ce-Ca-S* inclusions.

Table 2. Classification, percent of inclusion type, and chemical analysis (given in weight %) of each high Z-contrast inclusion in Heat 3 (*Ca+Ce* treated).

Inclusions	%	*N*	*Al*	*P*	*S*	*Ca*	*Ti*	*La*	*Ce*
Ca-Ce-S	69	2	4	0	24	20	0	19	31
Ce-S	6	11	13	2	14	3	0	19	36
Total sulfides	**75**								
Ce-Ca-P	2	2	5	19	4	6	0	5	58
Ce-P	20	2	8	30	2	0	2	2	50
Other with *P*	3	0	6	14	27	0	50	0	0
Total phosphides	**25**								
Total particles	100								

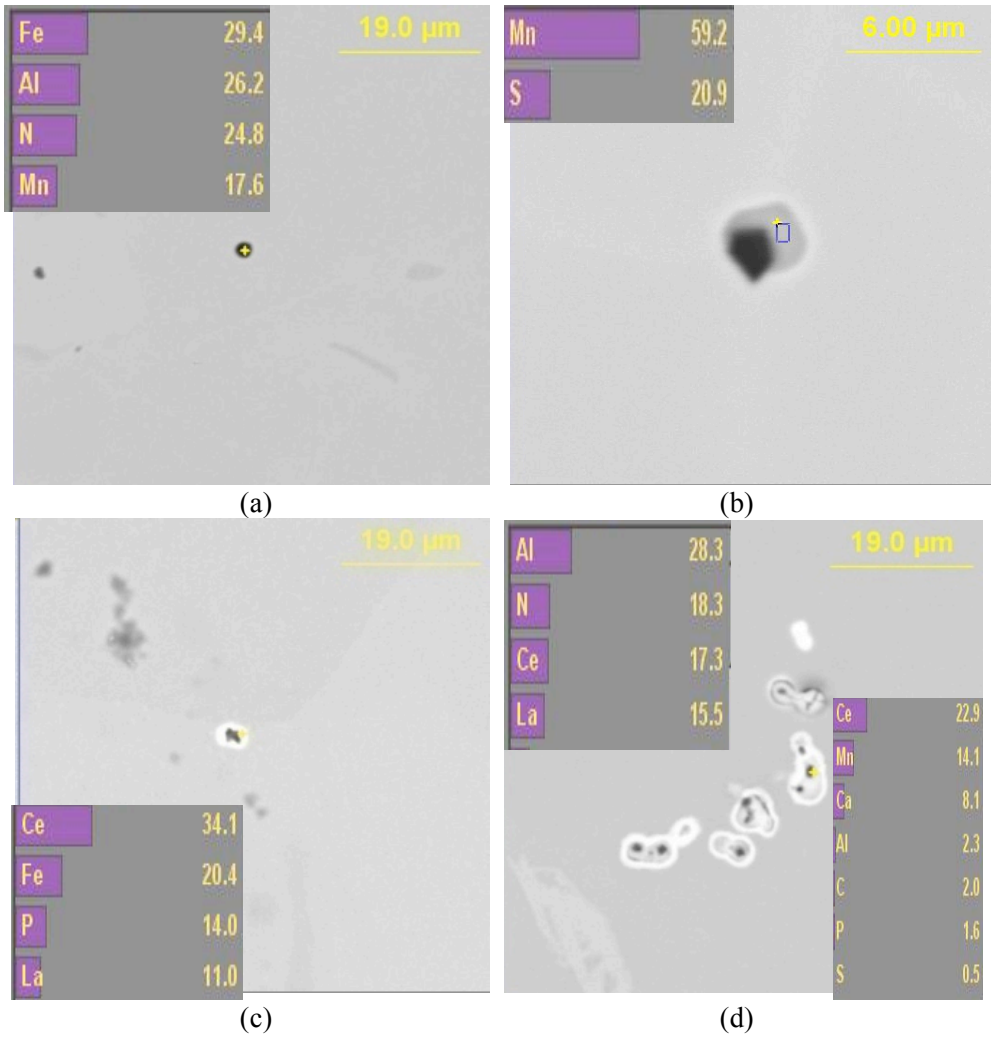

Figure 14. Inclusions in *Fe-Mn-Al-C* steel: base heat - *AlN* (a) and *MnS* with *AlN* core (b), *Ca+Ce* treated - REM with *P* inoculated by *AlN* (c) and aggregated complex REM-*Ca* with *P* having *AlN* core inclusions (d).

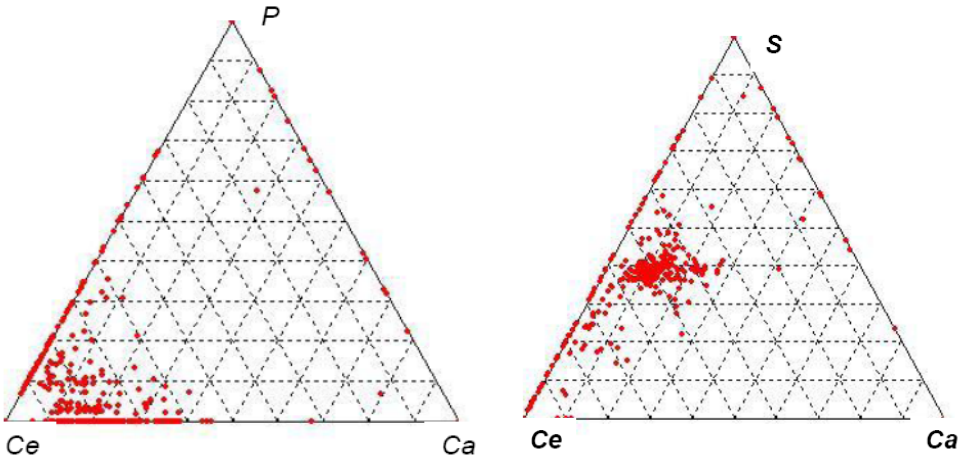

(a) (b)

Figure 15. Composition of (a) *Ce-Ca-P* and (b) *Ce-Ca-S* inclusions in *Ca+Ce* treated *Fe-Mn-Al-C* steel.

Automated feature analysis was performed using ASPEX PICA 1020 software to determine if the type of inclusion affects the CVN impact energy of *Fe-Mn-Al-C* alloys at -40°. The inclusion density of *AlN* particles was the only inclusion parameter showing a direct correlation to CVN impact energy (see Figure 16). All other factors, including particle size, total inclusion density, and *P* content, were interrelated. For example, the industrial heat had large particles (see Figure 17) but a small total inclusion density (see Figure 18) and it outperformed all other heats. Heat 5 performed nearly as well as the industrial heat. The latter was very low in *P* content (0.001%), whereas Heats 1-4 had 0.030%*P* and Heat 5 had 0.017%*P*. Also, complete removal of *S* from the melt for misch metal treatment may do some harm since *MnS* tends to coat *AlN,* which may reduce crack initiation at the *AlN* inclusions. Thus, *P* mitigation through the addition of both *Ca* and *Ce* must be followed by *Ar*-stirring to remove *AlN*, or a suitable method to remove nitrogen must be employed during steelmaking to prevent the formation of *AlN*.

Overall steel cleanliness was investigated by measuring a large area (50 mm^2); and Figure 19 compares the number and size of inclusions in the *Ca*- and *Ce*-treated heats with *Ar*-stirring. Heat 4 was stirred with an *Ar* lance for 60 seconds and poured with a lip-pour ladle, whereas Heat 5 was stirred for 30 seconds, tapped into a teapot-style ladle, and *Ar*-stirred for an additional 15 seconds.

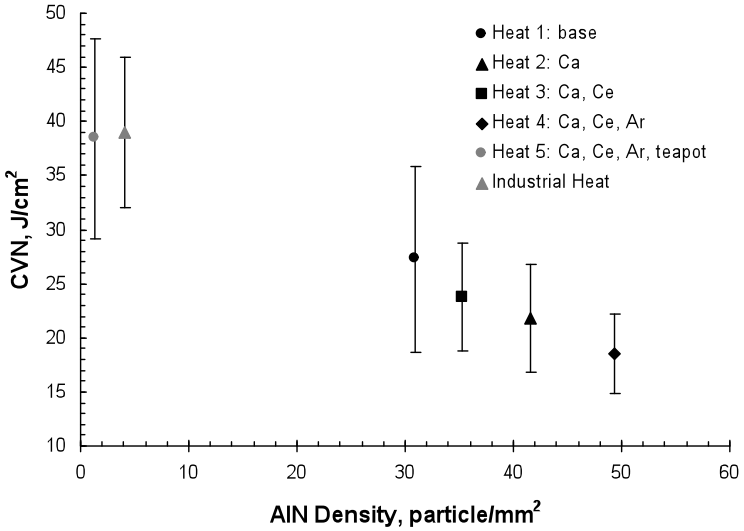

Figure 16. There is an inverse relationship between the *AlN* inclusion density and CVN impact energy.

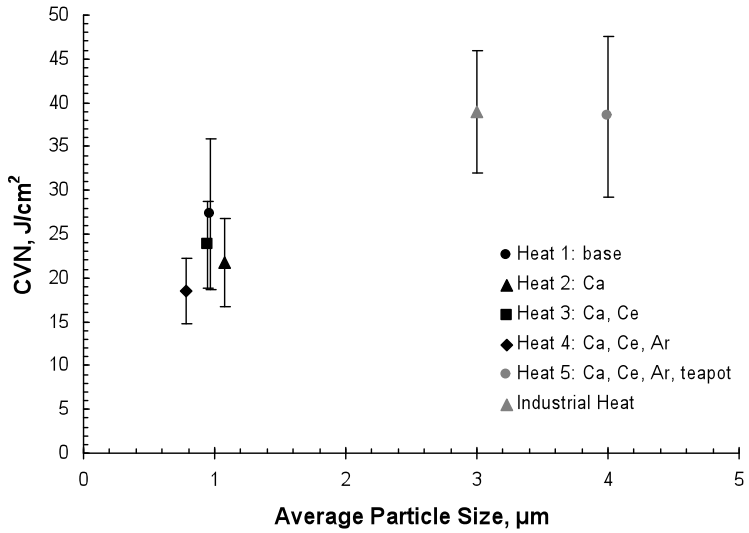

Figure 17. The impact energy is not directly affected by the average size of the inclusions. The data is grouped according to *P* content. The lowest impact energies are Heats 1-4 with 0.030wt.%*P*.

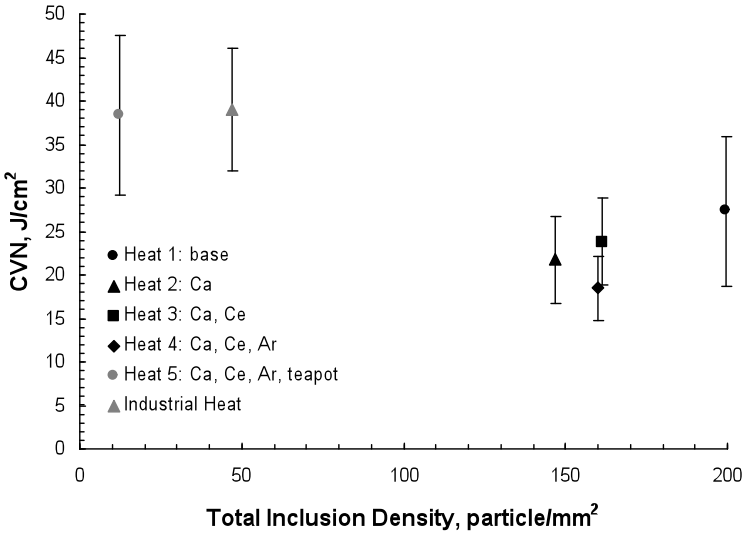

Figure 18. Total inclusion density in combination with *P* content affected the CVN impact energy. The lowest impact energies are Heats 1-4 with 0.030wt.%*P*.

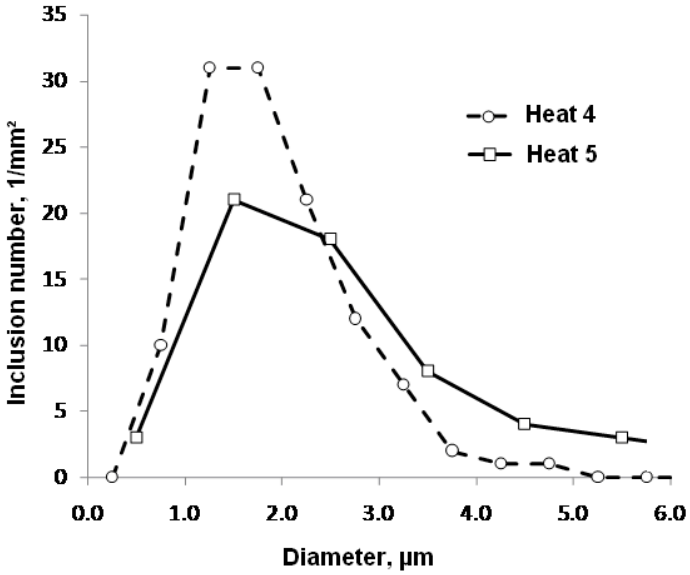

Figure 19. Inclusion size distribution in *Ca*+*Ce* treated heats using different *Ar*-stirring and ladling techniques.

Table 3 gives CVN results. Heat 2 (*Ca* treated) had fewer inclusions than the untreated Heat 1. The *Ce* treatment in Heat 3 created small, high-density, REM-bearing inclusions. *Ar*-stirring in an open induction furnace did not significantly affect inclusion content in Heat 4. For Heat 5, the combination of 30 second *Ar*-stirring in the furnace, 15 second stirring in the ladle, and pouring from a teapot ladle decreased inclusion content by 94% when compared with the base heat. Room temperature CVN impact toughness correlated to *P* levels and inclusion content, specifically, *AlN* inclusion content. Sequential *Ca* and *Ce* treatment followed by *Ar*-stirring increased the CVN impact toughness at room temperature from 33.3 ± 2.3 J to 107.9 ± 8.2 J.

Table 3. Inclusion density and CVN results

Heat designation (treatment)	Inclusion density (N/mm^2)	Room Temperature		-40°	
		BHN	CVN (J)	BHN	CVN (J)
Heat 1 (base)	200	317.6 ± 10.0	33.3 ± 2.3	318.7 ± 13.9	27.3 ± 8.6
Heat 2 (*Ca)*	163	324.7 ± 13.9	81.4 ± 4.2	329.2 ± 14.2	21.8 ± 5.0
Heat 3 (*Ca, Ce)*	188	321.9 ± 17.6	71.2 ± 5.6	328.7 ± 23.1	23.8 ± 5.0
Heat 4 (*Ca, Ce, Ar*-stir)	210	309.4 ± 21.3	91.8 ± 5.7	320.0 ± 11.0	18.5 ± 3.7
Heat 5 (teapot ladle)	12	335.1 ± 11.7	108 ± 8.2	336.4 ± 5.7	38.4 ± 9.2

Fractography of Charpy bars tested at room and low temperature are shown in Figures 20 and 21, respectively. Microvoid coalescence dominated the fracture surface with void nucleation at nonmetallic inclusions, which were predominantly *AlN*. These inclusions are most visible in Figure 20a in the microvoids of the fracture surface. In contrast, at -40° the fracture exhibited evidence of intragranular cleavage. For example, the base and *Ca* treated heats exhibited a combination of ductile and transgranular cleavage fracture (see Figure 21a-b). The *Ca*- and *Ce*-treated heat (see Figure 21c) exhibited ductile and brittle fracture, and the 60 second *Ar*-stirred, *Ca*-, and *Ce*-treated heat (see Figure 21d) exhibited intergranular cleavage. The 30 second *Ar*-stirred, *Ca*- and *Ce*- treated heat (see Figure 21e) exhibited a combination of ductile and cleavage fracture, which was mostly transgranular.

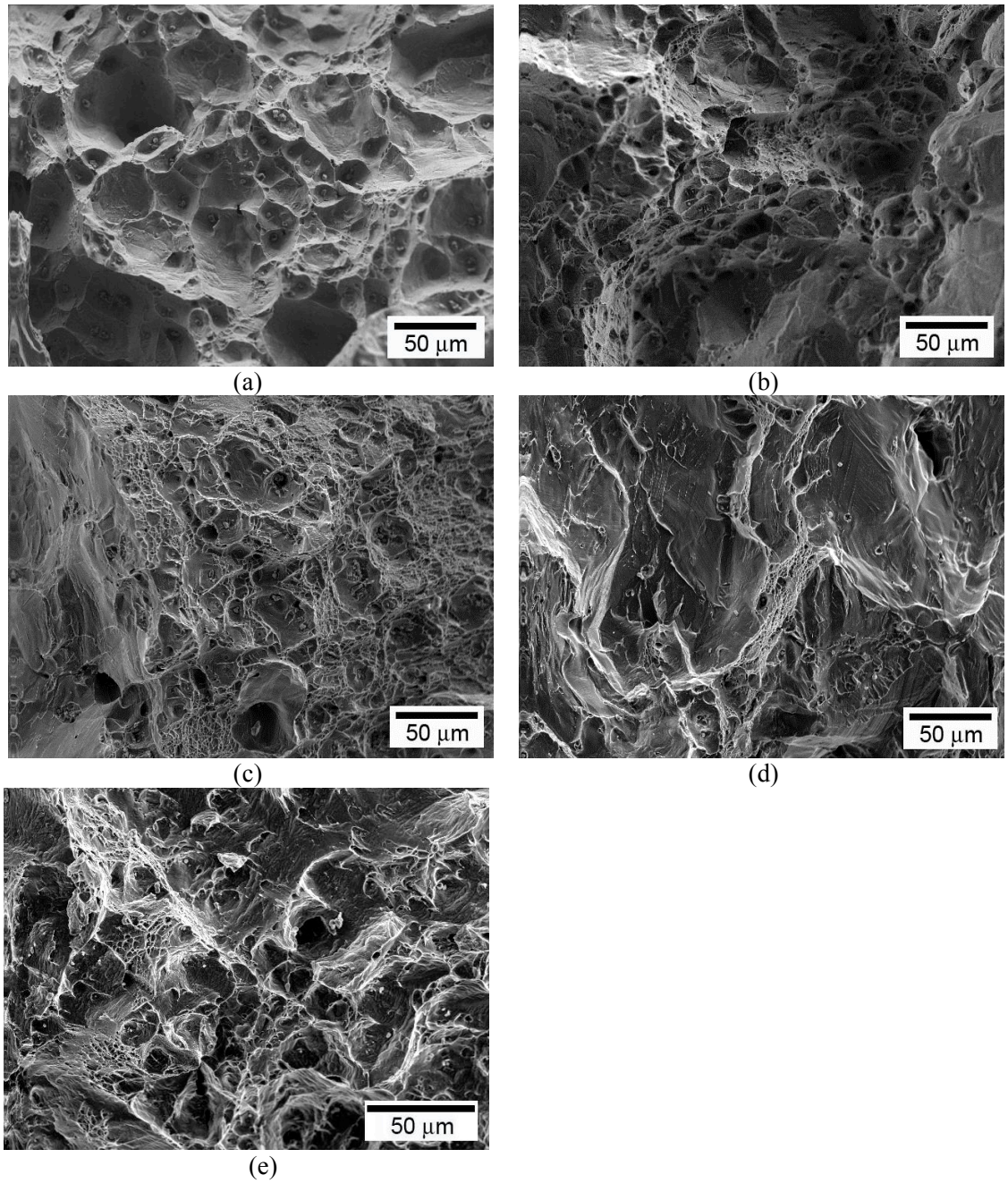

Figure 20. Fracture surfaces from CVN impact bars aged for 20 hours at 530°C (986ºF) and tested at room temperature were from the base heat (a), the *Ca*-treated heat (b), the *Ca*- and *Ce*-treated heat (c), the *Ar*-stirred heat after *Ca* and *Ce* treatment (d), and the double *Ar*-stirred heat after *Ca* and *Ce* treatment (e). All bars exhibited ductile fracture. *AlN* particles were clearly visible in the microvoids of the base heat (a).

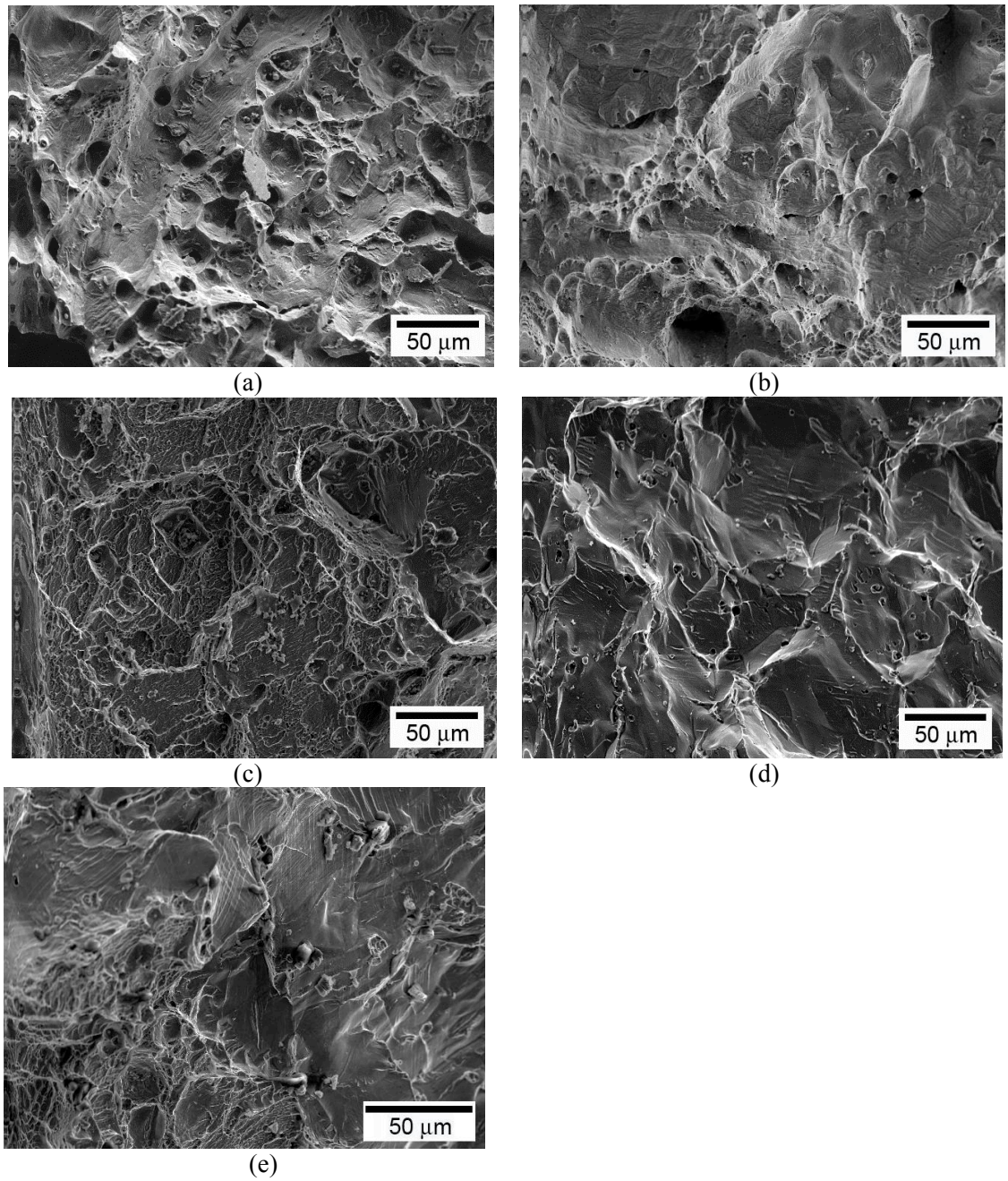

Figure 21. Fracture surfaces from CVN impact bars aged for 20 hours at 530°C (986ºF) and tested at -40° were from the base heat (a), the *Ca*-treated heat (b), the *Ca*- and *Ce*-treated heat (c), the *Ar*-stirred heat after *Ca* and *Ce* treatment (d), and the double *Ar*-stirred heat after *Ca* and *Ce* treatment (e). A combination of ductile and transgranular fracture was exhibited in the base and *Ca* treated heats (a,b). The *Ca*- and *Ce*-treated heat exhibited ductile fracture (c) and the *Ar*-treated *Ca*- and *Ce*-treated heat exhibited intergranular cleavage (d). The double *Ar*-treated *Ca*- and *Ce*-treated heat exhibited a combination of ductile and cleavage fracture.

DISCUSSION

Precipitation hardenable *Fe-Mn-Al-C* alloys produce a wide range of mechanical properties that make this system attractive for the transportation industry. However, the *Fe-Mn-Al-C* system suffers from low CVN impact energy when the *P* content increases from a very low level (0.001-0.005%) to more than 0.010-0.015%*P*[11]. Bartlett et al.[12] demonstrated experimentally that *P* promotes the formation of Fe_3AlC (κ-carbide) and decreases the time to peak aging. Medvedeva et al.[13] investigated the effect of *P* addition on brittle fracture in κ-carbide using first-principle electronic structure calculations. They predicted that *P* would facilitate both the intergranular and transgranular cleavage fracture of κ-carbide and postulated that each of these mechanisms relates to the electronic properties. They compared the binding energies for *P* substitution in bulk Fe_3AlC crystal, *P* monolayer at the Fe_3AlC surface, and *P* at the Fe_3AlC/γ-*Fe* interface. Their work showed that *P* has a strong tendency to segregate to the Fe_3AlC surface. Further, *P* substituted for *Al* in bulk Fe_3AlC sharply reduces, by 50%, the cleavage fracture energy of κ-carbide. Further, a strong anisotropy of *Fe-P* bonds in Fe_3AlC arises under tensile stress, resulting in the appearance of structural voids and facilitating the cleavage fracture. These first-principle calculations provided important information about the mechanism of *Fe-Mn-Al-C* embrittlement.

The present study shows that *P* mitigation can be attained by reacting *P* with additions of *Ca* and misch metal, and the resulting best practices of Heat 5 compare favorably with an industrial heat with low *P* content (0.001wt%).[11] The industrial heat was refined with *Ca* in three additions and deslagged after each addition. *Ar*-stirring was employed throughout the refining process, and teapot style ladles were used for the industrial castings. Comparison of the industrial heat to higher-*P* heats cast for this study shows a dramatic improvement in notch toughness when *Fe-Mn-Al-C* steel had only 0.001%*P*. In addition to low *P* content, the industrial alloy had one-fourth the inclusion density of Heats 1 and 4 (see Table 4). The inclusion density in this steel was 47 inclusions/mm^2. Previous studies on inclusion floatation and resultant inclusion population in medium carbon steel have shown that increasing ladle size and melt holding time significantly improves steel cleanliness[14].

CVN samples in the low *P* (0.001wt.%) industrial *Fe-30Mn-9Al-1Si-0.9C-0.5Mo* alloy had an impact toughness of 115 J at room temperature and 39 J at -40°, whereas base laboratory Heat 1 with 0.03%*P* had only 33 J at room temperature and 27 J at -40° (see Table 4). Both high *P* and high inclusion content reduced CVN impact energy at room temperature and at -40°.

Table 4. Inclusion density, hardness, and CVN toughness comparison of laboratory heats and low-*P* industrial heat.

Heat designation (treatment)	Inclusion density (N/mm^2)	Room Temperature CVN (J)	-40° CVN (J)
Heat 1 (base, 0.03%*P*)	200	33.3 ± 2.3	27.3 ± 8.6
Heat 4 (*Ca, Ce, Ar*-stir)	210	91.8 ± 5.7	18.5 ± 3.7
Heat 5 (teapot ladle)	12	107.9 ± 8.2	38.4 ± 9.2
Industrial[11] heat (0.001% *P*)	47	114.6 ± 6.7	39.2 ± 7.5

Refinement with *Ca* and *Ce* additions increased room temperature toughness whereas all untreated and treated alloys had a low CVN impact energy at -40°. Melt cleanliness was the main problem in the first four heats; it was a result of reoxidation of the melt and inclusion entrapment during ladle pouring.

Mitigation of *P* and *S* in the *Fe-Mn-Al-C* melt depends on removal of *Ca* and *Ce* reaction products produced during refinement or on protecting these products from reoxidation. In this regard, the *Ca* and *Ce* inclusions may aggressively react at the melt surface even during *Ar*-stirring if an incorrect stirring technique is applied, as in Heat 4. Tapping and pouring produces reoxidation of *Fe-Mn-Al-C* melt when there is a high rate of melt-gas surface reaction. The technique of lip-pouring used in the first four heats (see Figure 22a) did not allow separation of slag inclusions during casting. These problems were evident in the castings from Heat 4 (see Figure 23), which had large inclusions and oxide bi-films associated with micro-porosity in the casting drag. Low temperature toughness was very sensitive not only to *P* content but also to the total inclusion content.

To improve steel cleanliness, modified *Ar*-stirring and ladling techniques were applied. Computational fluid dynamic (CFD) modeling showed that *Ar*-stirring has the potential to float the fine (micron size) inclusions from the small ladle in very short time, as shown in Figure 11. Improvements in *Ar*-stirring included shortening the stirring time from 60 to 30 seconds and applying a second *Ar*-stirring in the ladle. A lip-pour ladle with a ceramic dam (Figure 22b) was used instead of a simple lip-pour ladle. These process improvements dramatically increased the cleanliness of Heat 5 in comparison to Heats 1-4.

(a) (b)

Figure 22. (a) Lip-pour ladle used for Heats 1-4 and (b) teapot ladle used for Heat 5.

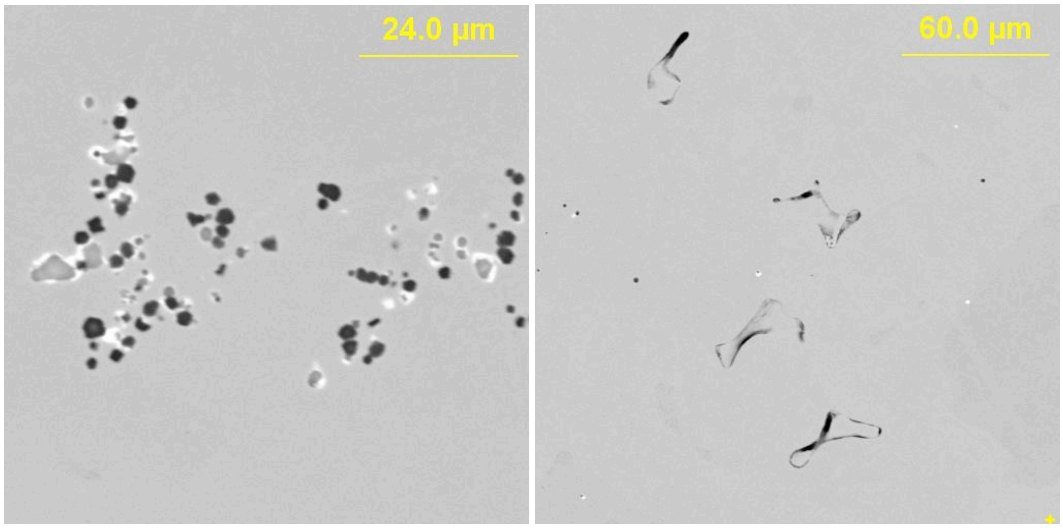

(a) (b)

Figure 23. Large segregation of complex inclusions (a) and bi-films associated with micro-porosity (b) in *Fe-Mn-Al-C* steel with *Ca*+*Ce* additions and *Ar*-stirred (Heat 4).

CONCLUSIONS

Thermodynamic and CFD models were used to design a metallurgical refining process for *P* mitigation in *Fe-30Mn-9Al-1Si-0.9C-0.5Mo* steel. The modeled treatment parameters were experimentally tested. Statistical analysis of non metallic inclusions in cast *Fe-Mn-Al-C* steel showed improvement in steel cleanliness and the possibility of mitigation of *P* embrittlement by formation of complex REM inclusions in the melt, which could increase the toughness of age-hardened *Fe-Mn-Al-C* steel. The sequential additions of *Ca* and *Ce* combine to mitigate *P* where the reactions with *S* and *O* have been completed. The addition of *Ar*-stirring in the small-capacity furnace did not always increase steel cleanliness. In particular, *Ar* stirring of *Ca*- and *Ce*-treated melts without atmospheric protection increased the inclusion content of the steel. The number of inclusions and *P* content affected the CVN impact toughness of *Fe-Mn-Al-C* steel. Significant improvements in notch toughness of *Fe-Mn-Al-C* steel were achieved by a combination of *Ca* and *Ce* treatment to mitigate *P*, and *Ar*-stirring to improve steel cleanliness.

ACKNOWLEDGEMENTS

This work was supported in part by the Leonard Wood Institute under the provisions of cooperative agreement W911NF-07-2-0062 with the Army Research Laboratory. The authors also gratefully acknowledge Waukesha Foundry, Inc. for providing the low-phosphorus Fe-Mn-Al-C alloy.

REFERENCES

1. Howell, R.A., Weerasooriya, T., Van Aken, D.C., "Tensile, High Strain Rate Compression, and Microstructural Evaluation of Lightweight Age Hardenable Cast Fe-30Mn-9Al-XSi-0.9C-0.5Mo Steel," *AFS Trans*. 117, pp. 751-763 (2009).

2. Sato, K., Tagawa, K., and Inoue, Y., "Modulated Structure and Magnetic Properties of Age-Hardenable Fe-Mn-Al-C Alloys," *Met. Trans A* 21A, pp. 5-11 (1990).

3. Howell, R.A., Lekakh, S.N., Van Aken, D.C., Richards, V.L., "The Effect of Silicon Content on the Fluidity and Microstructure of Fe-Mn-Al-C Alloys," *AFS Trans.* 116, pp. 867-878 (2008).

4. Howell, R.A., Lekakh, S.N., and Van Aken, D.C., "Quench Sensitivity of Cast Fe-30Mn-9Al-1Si-0.9C-0.5Mo Lightweight Steel," AISTech 2009 Proceedings Vol. II, pp. 681-698 (2009).

5. McMahon, C.J., Jr. "The Role of Non-Equilibrium Segregation in Impurity Segregation in Steels," *Scripta Materialia* 49, pp. 1215-1217 (2003).

6. Sevc, P., Janovec, J., Lejecek, P., Zahumensky, P., and Blach, J., "Thermodynamics of Phosphorus Grain Boundary Segregation in 17Cr12Ni Austenitic Steel," *Scripta Materialia* 46, pp. 7-12 (2002).

7. Schlesinger, M.E., "The Thermodynamic Properties of Phosphorus and Solid Binary Phosphides," *Chem. Rev*. 102, pp. 4267-4301 (2002).

8. Raghavan, V., "Ce-Fe-P (Cerium-Iron-Phosphorus)," *JPEDAV* 25, pp. 166-167 (2004).

9. Qin, L., Feng, G., and Xingyuan, Z., "Behaviors of Lanthanum and Cerium on Grain Boundaries in Carbon Manganese Clean Steel," *Journal of Rare Earths* 25, pp. 485-489 (2007).

10. Ohta, H., and Suito, H., "Effect of Nonrandomly Dispersed Particles on Austenite Grain Growth in Fe–10mass%Ni and Fe–0.20mass%C–0.02mass%P Alloys," *ISIJ International* 46, pp. 832-839 (2006).

11. Howell, R.A., Lekakh, S.N., Medvedeva, J.E., Medvedeva, N.I., and Van Aken, D.C., "Phosphorus and Thermal Processing Effects on Charpy V-Notch Impact Toughness of Lightweight Fe-30Mn-9Al-1Si-0.9C-0.5Mo Alloy Steel," *Met. Trans A*, submitted for publication.

12. Bartlett, L.N., Van Aken, D.C., and Peaslee, K.D., "Effect of Phosphorus and Silicon on the Precipitation of κ-carbides in the Fe-30%Mn-9%Al-X%Si-0.9%C-0.5%Mo Alloy System," *AFS Trans.* 118, submitted for publication.

13. Medvedeva, N.I., Howell, R.A., Van Aken, D.C., and Medvedeva, J.E., "Effect of Phosphorus on Brittle Fracture in κ–carbide," *Acta Materialia*, submitted for publication.

14. Singh, V., Lekakh, S., and Peaslee, K., "Using Automated Inclusion Analysis for Casting Process Improvements," 62nd SFSA T&O Conference (2008).

PAPER

2. Modeling for Improved Casting Quality of High-Aluminum Steels

Angella M. Schulte, Simon N. Lekakh, Von L. Richards, David C. Van Aken

Missouri University of Science and Technology

Department of Materials Science and Engineering

Rolla, Missouri 65409

Tel: 573-341-4730

E-mail: vonlr@mst.edu

Accepted for publication in the Transactions of the American Foundry Society 2010.

ABSTRACT

High-strength, low-density, precipitation-hardened *Fe-Mn-Al-C* cast steel is a very attractive material for many weight-limited transportation applications and military armor. These types of cast components typically have a high surface-to-volume ratio and limited wall thickness. Liquid *Fe-Mn-Al-C* alloys have significantly different casting characteristics than regular carbon steel, in particular a strong tendency to re-oxidize and form surface films during the mold fill. These melt properties promote the formation of oxide film laps and cold shuts in thin-walled castings. This study modeled solidification with MAGMASOFT (Modeler 1) and FLUENT (Modeler 2) software and performed experiments to study the castability of *Fe-Mn-Al-C* steel P900 armor plates. The effect of superheat and venting procedures was evaluated for various molding techniques, including bonded olivine sand molds tilted at both 0º and 15º from the horizontal and pre-heated investment shell molds in the vertical orientation with a bottom-filled gating system. Modeling results were experimentally verified, and the optimal process parameters were determined. The best castings were produced in vertically oriented bottom-filled ceramic investment shell molds with a superheat of 300C° (540F°) and poured directly from the furnace into a preheated investment shell at 800°C (1472°F). Successful P900 castings were also obtained from the tilted bonded olivine sand molds when poured with a superheat above 300C° (540F°).

INTRODUCTION

P900 is a class-2 cast steel armor[1] with a required hardness of 302-352 Brinell hardness number (BHN). P900 is designed to be 50% lighter than a solid plate of equal dimensions. This reduction in weight is achieved by oblong holes in a staggered stacking sequence across the entire plate. This sequence produces a series of T-junctions in the casting (see Figure 1). The holes are at an oblique angle of 25° to deflect and break up ballistic threats[2]. Filling the intricate honeycomb pattern is a challenge, but high quality production castings have been successfully produced from 4130 steel. P900 armor has also been cast from lightweight steels with a 14% lower density. Lightweight *Fe-Mn-Al-C* steels also have a low melting temperature and good fluidity,[3] and they do not require expensive alloys such as nickel, cobalt, or chromium. *Fe-30Mn-9Al-1Si-0.9C-0.5Mo* alloys are solution treated, then quenched and age-hardened by precipitation

of the κ-carbide[4], *(Fe,Mn)$_3$AlC*. A fully austenitic microstructure is achieved after a two hour solution treatment above 950°C (1742°F). Peak hardness is achieved by aging at 530°C (986°F) for 30 hours. During aging, the hardness increases from 224 BHN to 372 BHN, tensile strength increases from 687 MPa to 1,065 MPa, and elongation to failure decreases from 44 to 8%. The addition of 1% *Si* improves ductility in peak-aged materials by preventing the formation of the *β-Mn* phase[3].

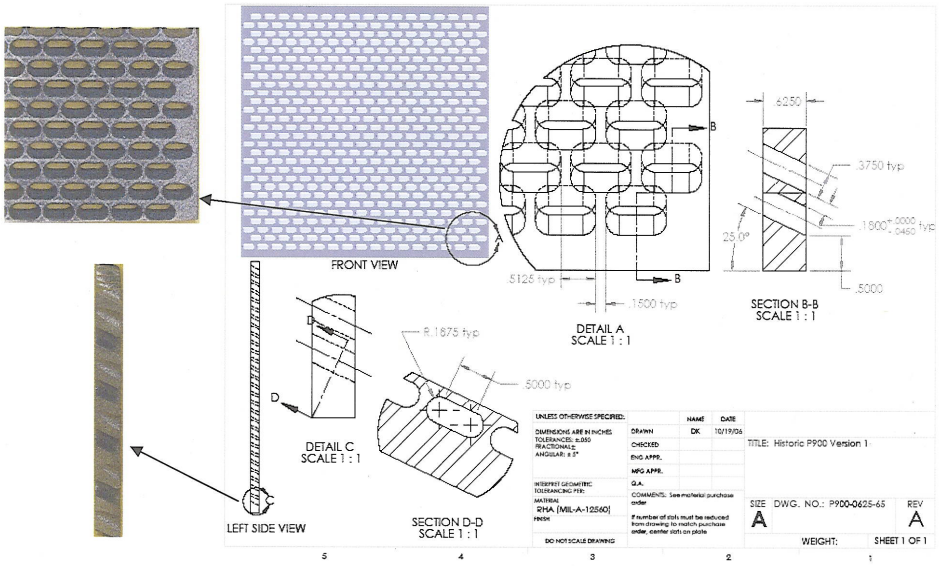

Figure 1. Image and the 2-D dimensional specification drawing of cast P900 armor plate.

During mold filling, the melt stream in a P900 mold experiences multiple direction changes, divisions, and merges. This mold geometry promotes the formation of cold shuts, that is, discontinuities that form due to imperfect fusion where two streams of metal converge[5,6]. Cold shuts are characterized by rounded seams that may exist only on the surface or may continue through the thickness of the casting[5,6]. They form due to one or a combination of the following: insufficient fluidity, oxidized metal, slow or interrupted pouring, or insufficient venting[5,6]. The high *Mn* (30wt.%) and *Al* (9wt.%) content promotes the formation of oxidation laps. The melt velocity controls the formation of oxidation laps. If there is an interruption of flow during filling, the oxide layer at the leading edge of the melt is no longer controlled by splitting and regrowth[7]. The oxide layer then thickens and imperfect fusion occurs when two streams converge, resulting

in a confluence weld containing an oxide film. Multi-hit capabilities of P900 armor are adversely affected by cold shuts and oxide film laps (see Figure 2) because they cause through-cracking.

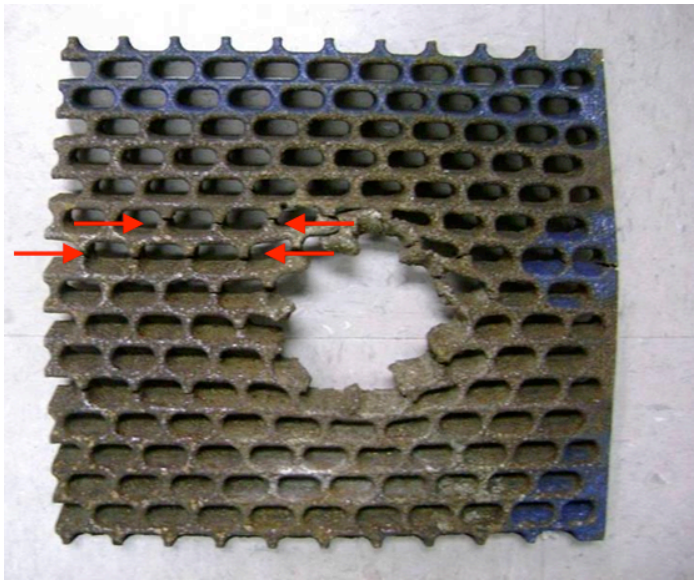

Figure 2. Arrows indicate through-cracking caused by cold shuts on this P900 ballistic test plate.

This study modeled the effect of three process parameters: superheat, venting, and melt velocity. It verified experimentally the tendency to form temperature- and oxidation-related defects by casting lightweight steel of nominal composition of *Fe-30Mn-9Al-1Si-0.9C-0.5Mo*.

DESIGN OF EXPERIMENTS

Modeling and experiments were performed with two different metal casting processes. The first process used bonded olivine sand molds in two orientations: a horizontally oriented P900 mold and a P900 mold tilted 15° from horizontal. The bonded olivine sand mold produced a P900 plate of 38.1 x 38.1 x 1.6 cm. The horizontally bonded olivine sand mold was modeled without venting, whereas the 15° tilted (x-z plane) bonded olivine sand mold was modeled with venting along the y-axis (back). The second process used a preheated ceramic shell that was built by investing a wax-coated evaporative foam pattern measuring 38.1 x 30.5 x 1.6 centimeter with

a bottom-filled gating system. The ceramic shell mold was modeled with an 800°C (1472°F) preheat and without venting. All mold designs were modeled in a range of superheats from 100 to 300C° (180 to 540F°). Results from the 100C° (180F°) and 300C° (540F°) superheat simulations were chosen as most representative; they are reported below.

In Modeler 1, the preprocessor was used to set up the mold and gating systems. The P900 patterns were imported as stereolithography files. Mold, vents, and an inlet were subsequently added to complete the model. All mold designs had a mesh generated with 2,000,000 elements; and each model had only three thin-walled elements and no blocked elements. A minimum of three layers of mesh was generated across all areas that experienced metal flow. The mesh parameters were set to default, and the values were as follows: wall thickness 5, accuracy 3, element size 5, smoothing 2, and ratio 5. For the investment process, the ceramic shell molds were modeled with a shell thickness of 7 mm and the thermal properties of silica sand. The grid consistency was verified after generation in each case. A user database (i.e., user created) specific to the *Fe-30Mn-9Al-1Si-0.9C-0.5Mo* alloy thermal properties was input (see Table 1). The liquidus (1350°C, 2462°F) and solidus (1290°C, 2354°F) temperatures and latent heat (260 kJ/kg) of the *Fe-Mn-Al-C* were taken from Howell et al.[3] (see Figure 3). All other sand mold and shell properties were taken from the Modeler 1 database. Filling time was set to 14 seconds for the bonded olivine sand molds, and the ceramic shell mold fill time was set to 10 seconds. Both values were based on experimental observation.

Solver 4 in Modeler 1 was used for the simulations. Solver 4 uses a more conservative approach than Solver 3, resulting in smaller time steps and more stable calculations. Data storage was set to automatic so that the result files were generated at 10%, 50%, and 90% solidification of the casting. Feeding effectivity describes the solidified fraction of the melt up to which macroscopic feeding can occur. The feeding effectivity is usually expressed as a percent and is strongly dependent on the solidification morphology. Columnar solidification morphologies have a higher feeding effectivity. A feeding effectivity value of 33% for *Fe-Mn-Al-C* steel was taken from dendrite coherency point calculations done by Howell et al.[3]

Three parameters were examined using Modeler 1 simulations to determine the possible causes and locations of cold shuts. These parameters included temperature distribution, air pressure, and melt velocity. The temperature distribution at 100% filled was examined. The air pressure results indicated areas of trapped air that prevent normal filling. Air pressure at 100% filled was also examined at each superheat and mold design. Velocity results helped identify any unintentional chokes by indicating areas of high velocity. They were examined at 40% and 80% filled for each mold orientation and superheat.

Table 1. *Fe-Mn-Al-C* latent heat values added to the Modeler 1 user database.

Temperature (°C)	Lambda (W/mK)
1.00	14.00
100	13.95
200	13.77
300	13.47
400	13.09
500	12.69
600	12.28
700	11.89
800	11.29
900	11.42
1100	11.66
1200	11.90
1290	12.05
1350	11.60
2000	11.76

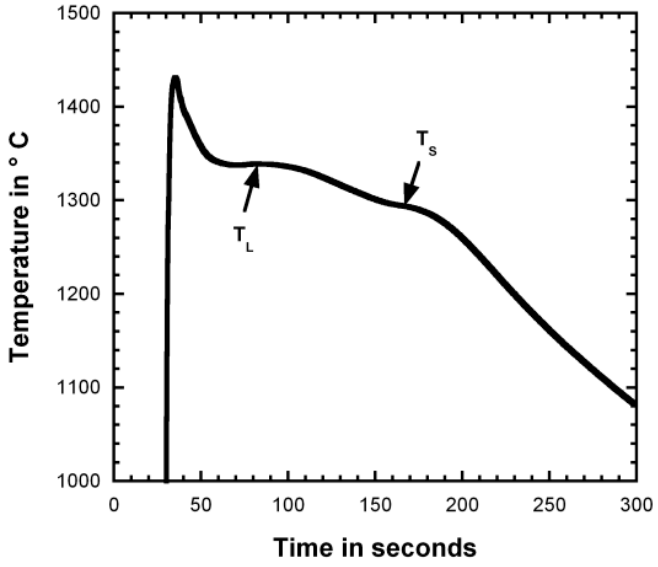

Figure 3. Cooling curve for *Fe-30Mn-9Al-1Si-0.9C-0.5Mo* alloy that highlights the liquidus (T_L) and solidus (T_S) temperatures[3].

MODELING RESULTS

Figure 4 shows temperature distributions in horizontal bonded olivine molds cast at different superheats. At a 100C° (180F°) superheat, the temperature distribution shows that over 90% of the P900 plate was at or near the liquidus temperature, and some volumes were in the liquid-solid region. At a superheat of 100C° (180F°) the P900 plate would have an incomplete fill or severe cold shuts.

In the mold cast with a 300C° (540F°) superheat, the temperature distribution in the whole mold cavity was above the liquidus temperature at 100% filled.
The gating system had the highest temperatures at 100% filled. The temperature distribution indicated decreasing temperatures as the metal approached the center of the plate. At the coldest points in the mold the temperatures were approximately 1410°C (2570°F), 60C° (108F°) greater than the liquidus temperature. At 300C° (540F°) superheat the P900 plate should not suffer from temperature-related defects.

Air pressure in the horizontally cast bonded olivine sand mold was also examined at 100C° (180F°) and 300C° (540F°) superheats (see Figure 5). Both simulations show large areas of high pressure in the P900 plate that indicate trapped air, which generally correlate with cold shuts[8]. The large white areas in the figures indicate pressures higher than 1020 mbar.

Figure 6 shows the velocity simulation results for the horizontally cast mold design. The velocity of the liquid metal, as well as the path traveled by the melt, was examined at 40% and 80% of mold fill at 100C° (180F°) and 300C° (540F°) superheats. The molten steel filled the outer runners first, before moving inward to fill the webbed sections from bottom to top. This order of filling may explain the air pressure distribution (see Figure 5). At 40% filled, the velocity in both the 100C° (180F°) and 300C° (540F°) superheat simulations was high where the metal encountered the narrow gates that lead into the mold cavity. High velocity can produce jets of liquid metal that cause excessive exposure to air, leading to oxidation. At 80% filled, the highest velocity was still in the runners, but the flow in the plate was 75% less turbulent than when the mold was 40% filled. Both the 100C° (180F°) and 300C° (540F°) superheat simulations would experience oxide-related defects due to the initial jetting effect.

These simulations indicated that P900 plate produced in horizontally cast bonded olivine sand mold could suffer severe casting defects. The industrial practice of producing P900 in the horizontal would have a series of mold vents running down the center of the mold and parallel to the runners.

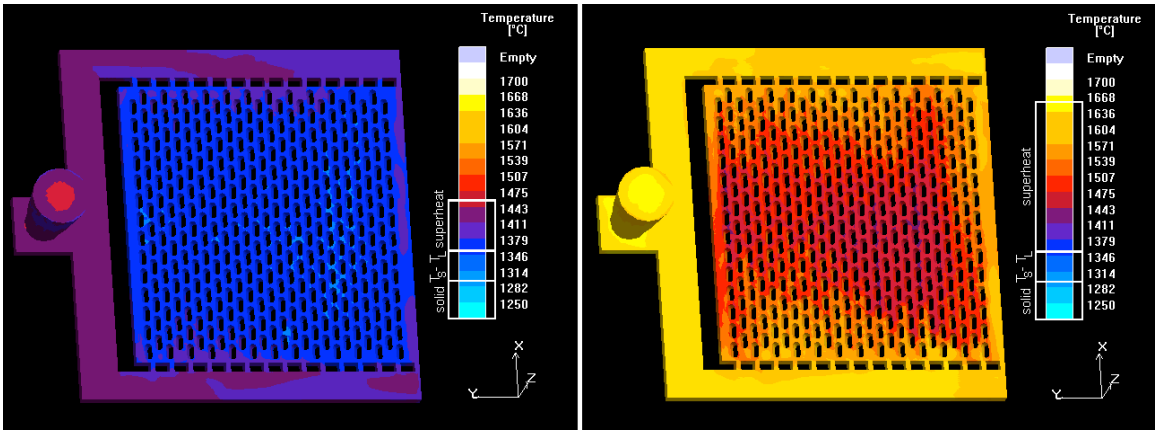

(a) (b)

Figure 4. Horizontally cast bonded olivine sand simulation was compared at superheats of 100C° (180F°) (a) and 300C° (540F°) (b). The 100C° (180F°) superheat (a) simulation showed that more than 90% of the plate was at or near the liquidus temperature (indicated by dark blue), and the regions indicated by light blue were in the liquid-solid region. The 300C° (540F°) superheat (b) simulation shows no areas near the liquidus temperature.

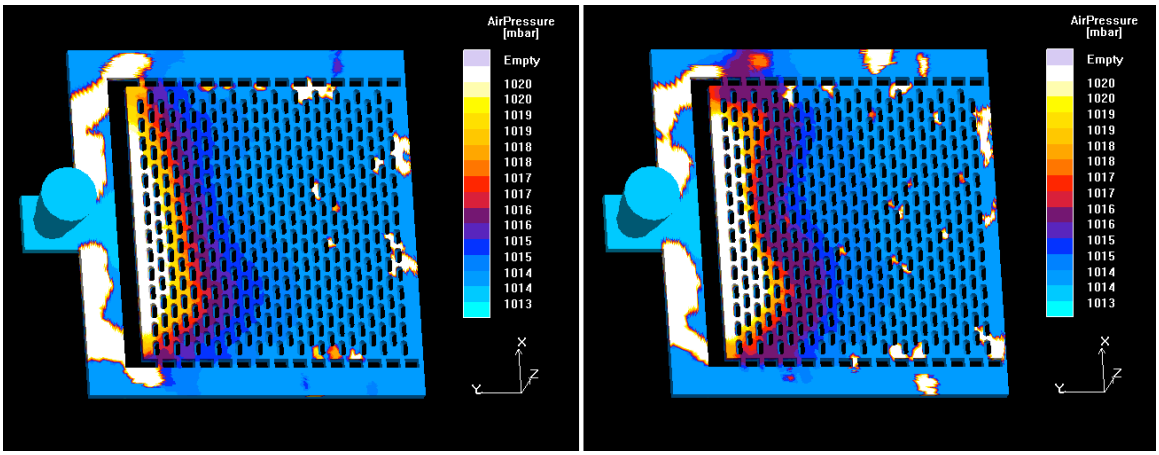

(a) (b)

Figure 5. Air pressure gradients of the horizontally cast bonded olivine sand mold simulations were compared between the 100C° (180F°) (a) and 300C° (540F°) (b) superheat models. The distribution of air pressure was similar in each model but greater in the 300C° (540F°) superheat (b) model.

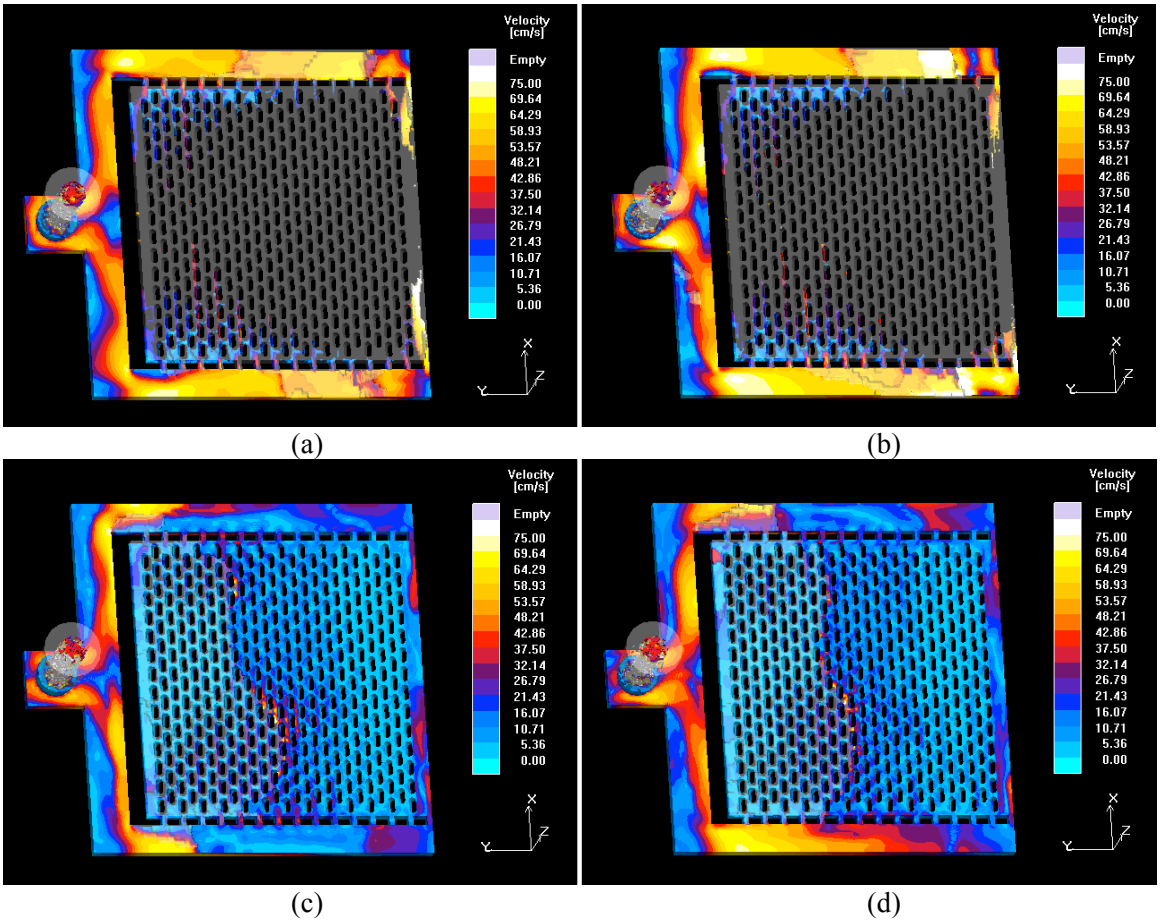

Figure 6. Velocity was modeled at two points in the horizontally cast bonded olivine sand mold for each superheat. Velocity at 40% filled was examined for the 100C° (180F°) (a) and 300C° (540F°) (b) superheats. Velocity at 80% filled was examined at 100C° (180F°) (c) and 300C° (540F°) (d) superheats. Filling was turbulent at the runners and led to excessive exposure to air.

To improve casting quality, the bonded olivine sand mold design was simulated with a 15° tilt, sloping up from a single in-gate. In addition to tilt, the mold cavity was vented along the back y-axis (see Figure 7). The temperature distribution for 100% filled mold was examined for both the 100C° (180F°) and 300C° (540F°) superheats (see Figure 8). The 100C° (180F°) superheat model indicated that 70% of the plate was at the liquidus temperature of 1350°C (2462°F). There were also regions, indicated by light blue, that were in the solid-plus-liquid regime. At 100C° (180F°) superheat, the P900 casting would have an incomplete fill or severe cold shuts due to insufficient superheat.

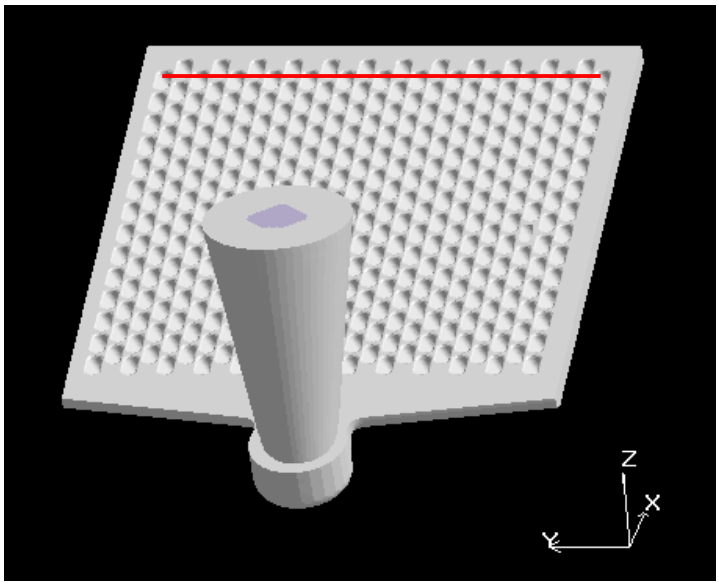

Figure 7. Modeler 1 postprocessor image of the vented P900 plate cast at 15º from horizontal. Five vents were evenly spaced every 6.35 cm along the red line.

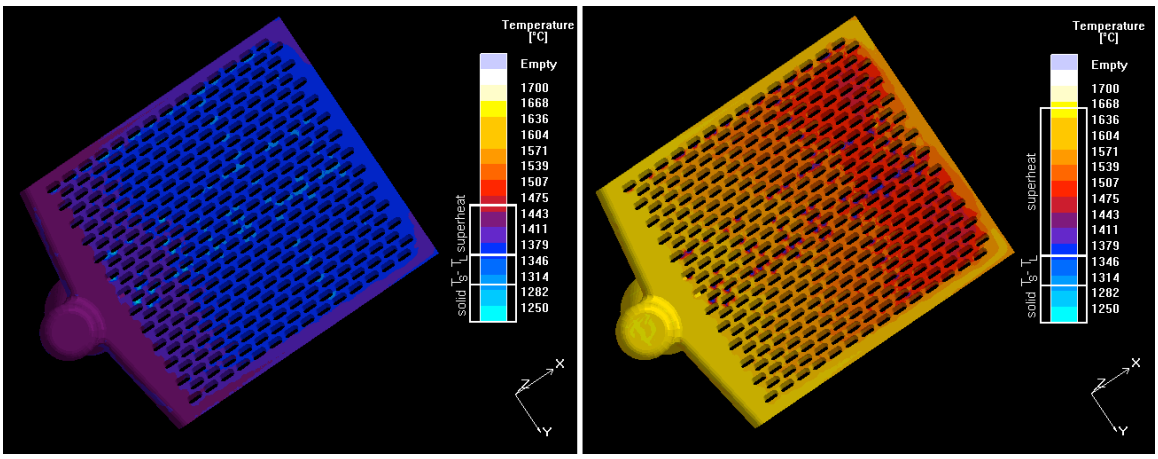

(a) (b)

Figure 8. The 15º tilt from horizontal, bonded olivine sand mold simulation was compared at 100C° (180F°) (a) and 300C° (540F°) (b) superheats. Seventy percent of the plate simulated at a superheat of 100C° (180F°) (a) was at the liquidus temperature (indicated by dark blue), and there were solid areas (indicated by light blue) present as well. The 300C° (540F°) superheat (b) simulation showed several areas near the liquidus temperature (indicated by dark blue), but the remainder of the plate was at least 100C° (180F°) above the liquidus.

The 300C° (540F°) superheat model indicated that the temperature distribution in the whole mold was at least 100C° (180F°) above the liquidus temperature at 100% filled, except for a region in the center of the cope side of the plate where the temperature was near 1350°C (2462°F), the liquidus temperature. At 300C° (540F°) superheat, the P900 casting may have cold shuts on the cope side in the center of the plate.

Air pressure simulations at both 100C° (180F°) and 300C° (540F°) superheats (see Figure 9) showed a significant decrease in air pressure and entrapped air compared with the horizontally cast mold design (see Figure 5). One small area of high pressure (indicated in gray) existed in each simulation, at each superheat. The horizontally cast mold had high-pressure areas across the front x-axis of the P900 plate. The 15º tilted mold simulation had much smaller areas of high pressure located near the vented areas (back y-axis). Insufficient vent size or vent number may cause the high pressure areas near the vents.

Velocity simulations showed that the liquid-air front in the tilted and vented mold (see Figure 10) was more uniform when compared to the horizontally cast mold design (see Figure 6). The fluid flow in the mold was more uniform due to the reduced volumetric flow rate and, as a result, there was less air-steel interaction than in the horizontal mold simulation. The 15º mold had a more stable fill, which is important in reducing the formation of oxidation products in high-aluminum steels. Simulations were performed at 100C° (180F°) and 300C° (540F°) superheats and 40% and 80% filled for each superheat (see Figure 10). Average liquid metal velocity did not differ significantly among superheats, but the maximum velocity was 30% lower with the 15° tilt than in the horizontally cast mold (see Figure 6). The fill pattern shown in Figure 10 may explain the high-pressure areas near the vents. The middle-back of the mold was the last to fill, and the vents in the middle were the same size as those on the sides, which may not have been large enough to handle the volume of air exiting the mold.

The simulations of resin-bonded olivine sand molds showed that casting the P900 plate could be improved by tilting the mold upward 15° from the in-gate. Cold shuts and other defects were present in the 15° tilted bonded olivine sand mold. Superheats of greater than 300C° (540F°) may be possible, but the high aluminum and manganese contents of the *Fe-Mn-Al-C* steels may reduce the refractory life of the furnace lining, subjecting the melt to higher oxidation rates.

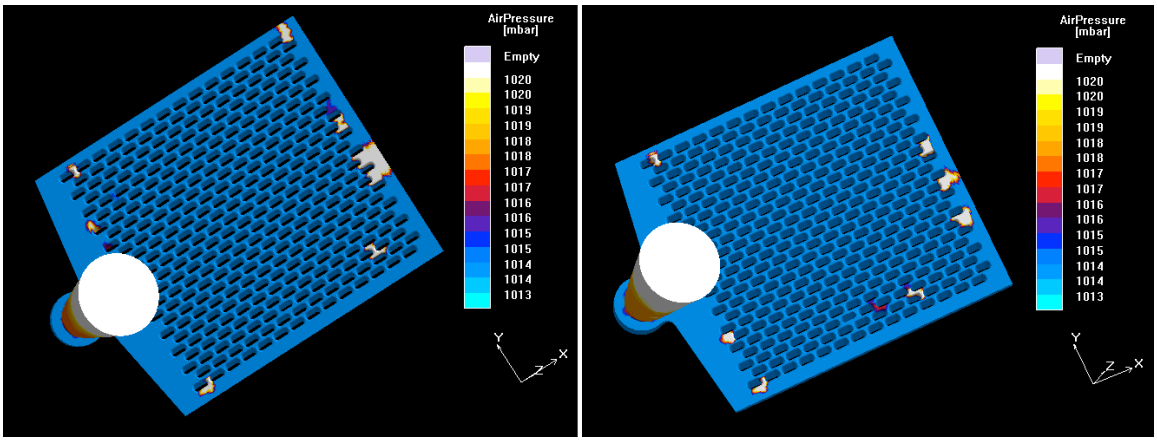

(a) (b)

Figure 9. Air pressure gradients of the 15º tilt, bonded olivine sand mold simulations were compared in the 100C° (180F°) (a) and 300C° (540F°) (b) superheat models. There was a section of high air pressure in each model near the vents, which indicates the vents should be larger or more numerous.

A ceramic shell mold was designed around an existing evaporative foam pattern of 30.5 x 38.1 x 1.6 cm. The foam pattern was coated with wax, invested with a ceramic shell, and subsequently burned out. The P900 plate mold was designed with gating at the bottom to promote a quiescent fill throughout the mold. The mold design was compared at 100C° (180F°) and 300C° (540F°) superheats, and the ceramic shells were preheated to 800°C (1472°F) (see Figure 11).

When poured at a superheat of 100C° (180F°), 38% of the P900 plate was near the liquidus temperature at 100% filled. This casting may have had some cold shuts in the region at the liquidus temperature. The 300C° (540F°) superheat model showed all areas were at least 150°C (302°F) above the liquidus temperature. No temperature-related defects would be expected in the 15° tilted P900 plate poured with 300C° (540F°) superheat.

Air pressure modeling results were compared at 100C° (180F°) and 300C° (540F°) (see Figure 12). Both models showed high-pressure areas at the top of the P900 plate, which was the last part to fill. The 100C° (180F°) model exhibited numerous high-pressure areas scattered throughout the webbed section of the P900 plate. The 300C° (540F°) model showed similar entrapped air areas, but there were fewer of them. The addition of vents along the top of the mold would reduce air pressure. Isolated high-pressure areas indicated locations of possible cold shuts or oxidation laps. There were fewer areas of concern in the 300C° (540F°) superheat model due

to the effect of temperature on melt viscosity. At temperatures near the liquidus, the melt viscosity rapidly increases and traps air.

The velocity at 40% filled was compared at 100C° (180F°) and 300C° (540F°) superheats (see Figure 13a-b). There was no significant difference between the velocity profiles. The highest velocities occurred in the gating, but the velocity decreased as the metal flowed upwards. At 80% filled (see Figure 13c-d), the velocities decreased 75% from the 40% fill. The bottom-filled mold design greatly decreased the melt velocity compared to bonded olivine sand molds (see Figure 6 and 10); as a result, it produced a less turbulent flow that prevented isolated low temperature areas.

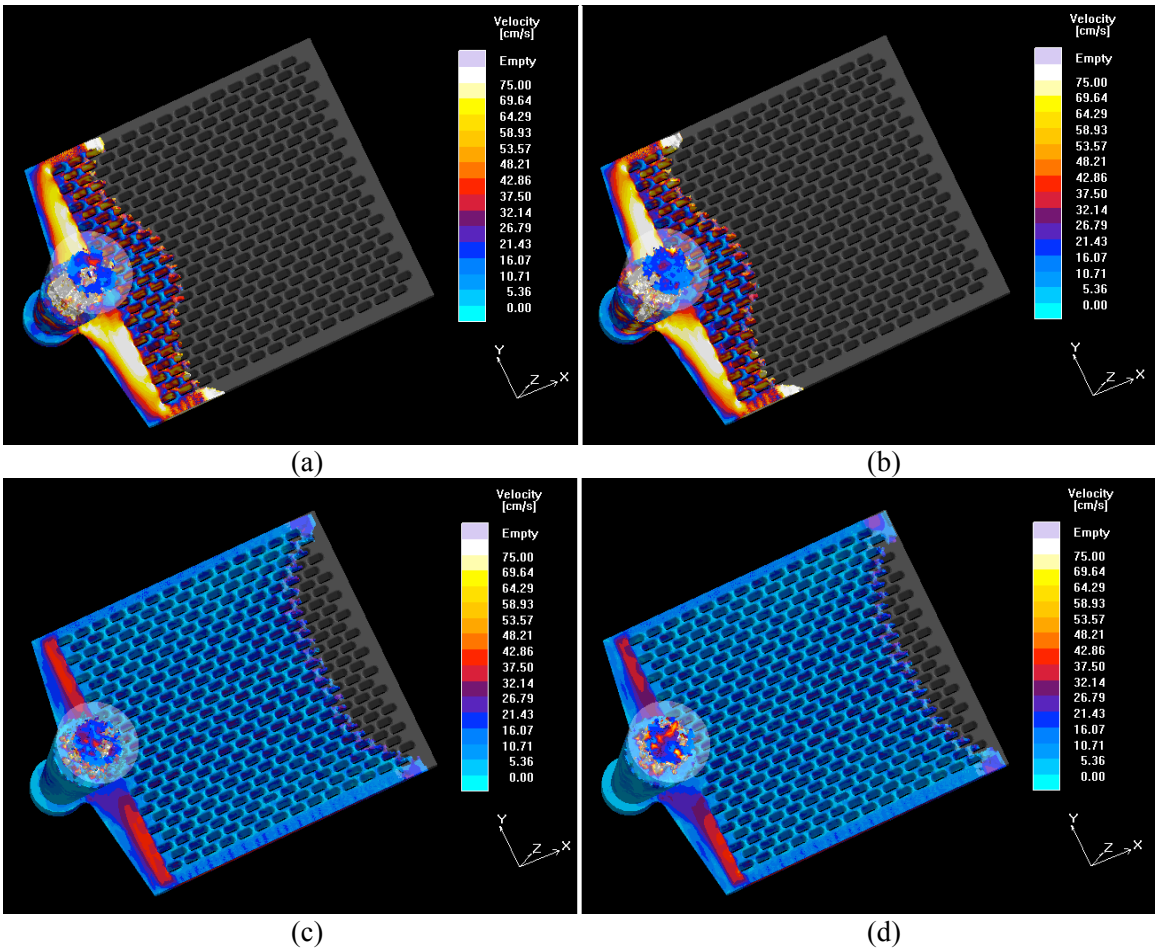

Figure 10. Velocity was modeled at two points in the 15º tilt bonded olivine sand mold for each superheat. Velocity at 40% filled was examined for the 100C° (180F°) (a) and 300C° (540F°) (b) superheats. Velocity at 80% filled was examined at 100C° (180F°) (c) and 300C° (540F°) (d) superheats.

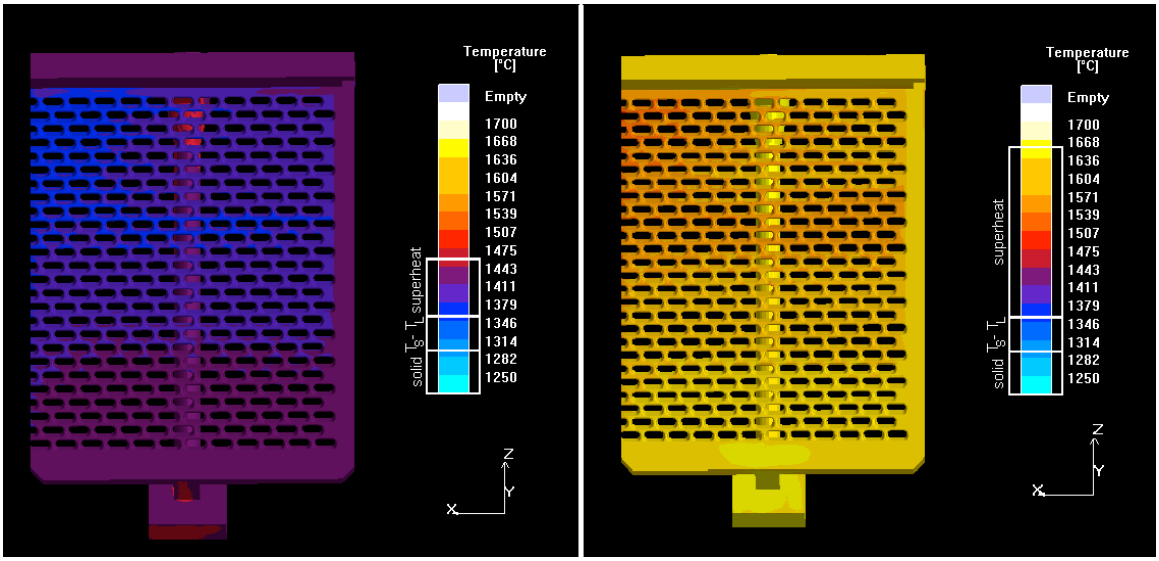

(a) (b)

Figure 11. The vertically cast preheated (800°C, 1472°F) ceramic shell mold simulation was compared at 100C° (180F°) (a) and 300C° (540F°) (b) superheats. The top section of the 100C° (180F°) superheat (a) simulation was at the liquidus temperature, but the 300C° (540F°) superheat (b) simulation showed a temperature distribution at least 150C° (270F°) above the liquidus temperature.

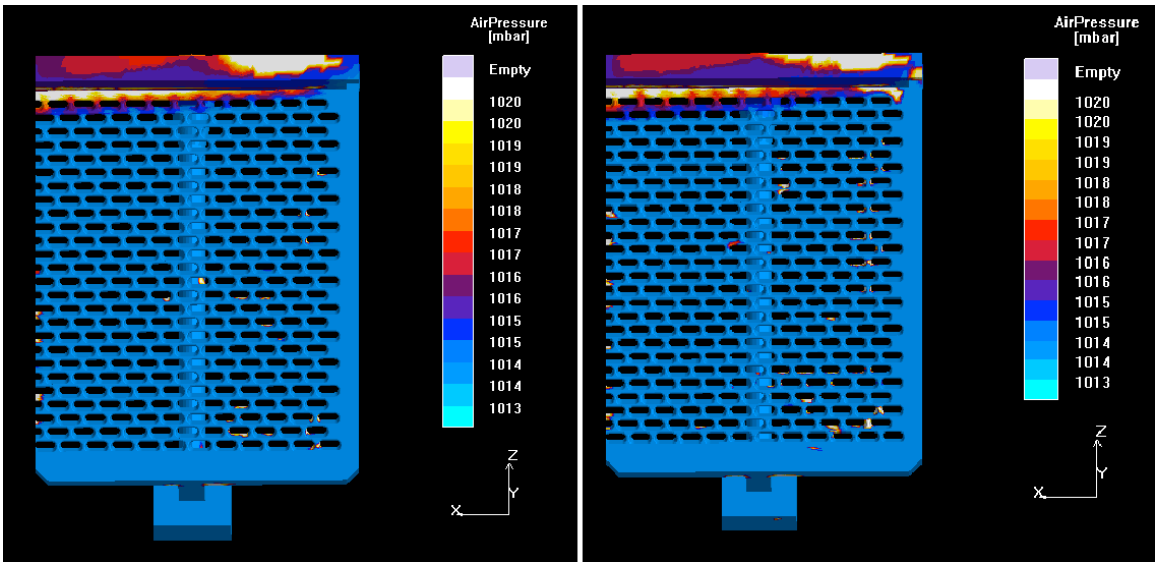

(a) (b)

Figure 12. Air pressure gradients in the vertically oriented preheated (800°C, 1472°F) ceramic shell mold were compared at 100C° (180F°) (a) and 300C° (540F°) (b) superheats. Both superheat conditions experienced high air pressure spots at the top of the mold, and the 100C° (180F°) superheat (a) contained areas of high pressure in the triple junctions of the P900 plate.

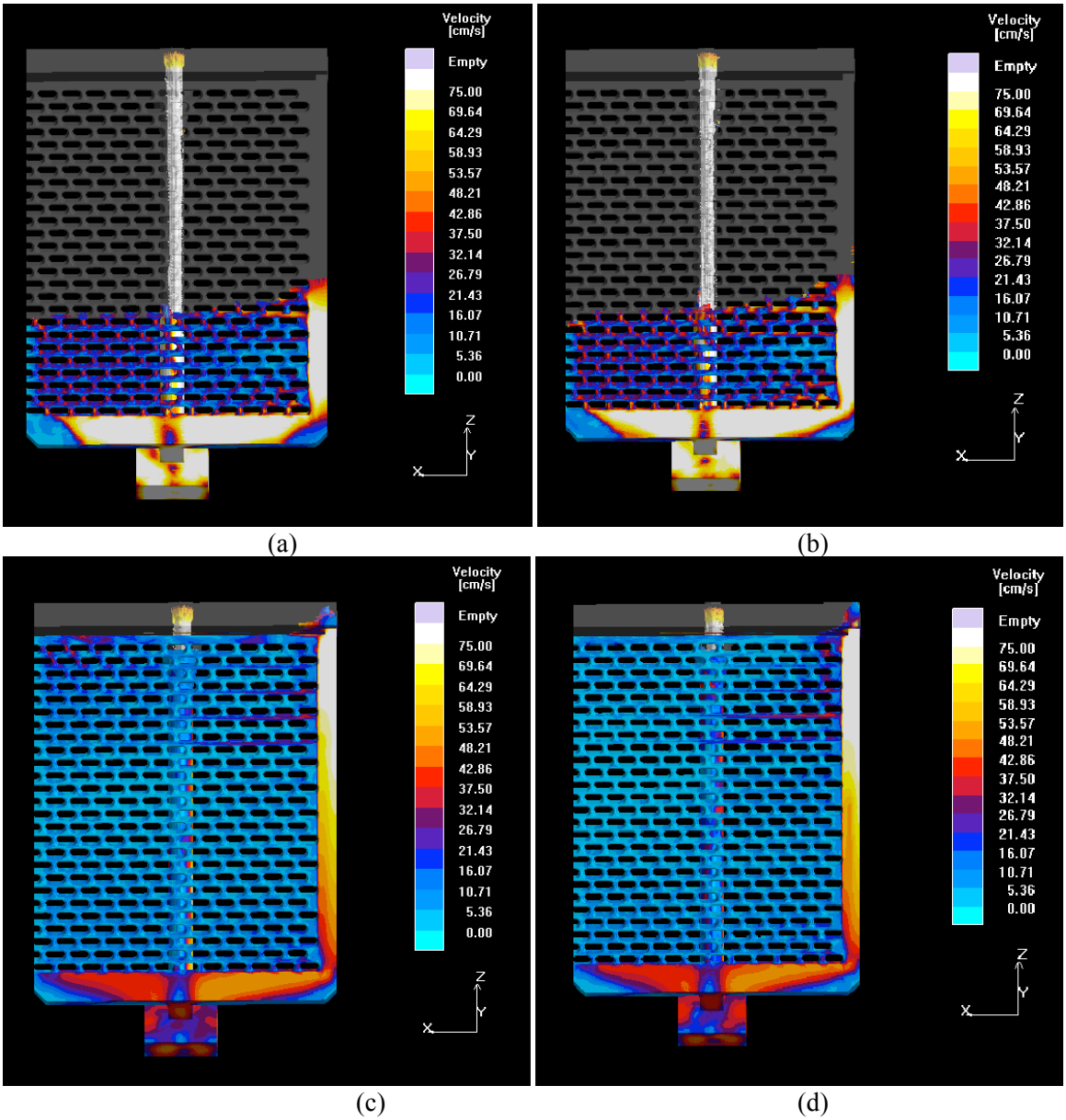

Figure 13. Velocity in the 100C° (180F°) and 300C° (540F°) superheat vertical filled preheated (800°C, 1472°F) ceramic shell molds at 40% filled (a,b) was much higher in the gating section of the P900 plate than it was in the 100C° (180F°) and 300C° (540F°) superheat molds at 80% filled (c,d).

EXPERIMENTAL RESULTS AND DISCUSSION

Three experimental heats of *Fe-30Mn-9Al-1Si-0.9C-0.5Mo* steel were produced in a 100 lb induction furnace with *Ar* protection, and corresponding Modeler 1 simulations were run for comparison. Figure 14 shows a P900 match-plate pattern and bonded olivine sand mold with a 15° tilt.

(a) (b)

Figure 14. Drag-side of P900 match-plate (a) and 15º tilt sand mold on specially designed pouring cart (b).

Three tilted bonded olivine sand molds were poured at 1631°C (2968°F), 1655°C (3011°F), and 1682ºC (3060°F), respectively, with 281C° (506F°), 305C° (549F°), and 332Cº (598F°) superheats, respectively. The results are shown in Figure 15. The P900 plates poured at 1631ºC (2968°F) and 1655ºC (3011°F) were vented along the center of the mold and completely filled, but they formed cold shuts. The plate poured at 1631ºC (2968°F) had more numerous and severe defects (see Figure 15a) than that poured at 1655ºC (3011°F) (see Fig 15b). The third plate was cast at 1682ºC (3060°F) and vented along the back. This P900 plate completely filled and had no visible cold shuts (see Figure 15c). These data correlate to modeling performed to match the poured plates (see Figure 16-17) and the initial modeling (see Fig 8-10).

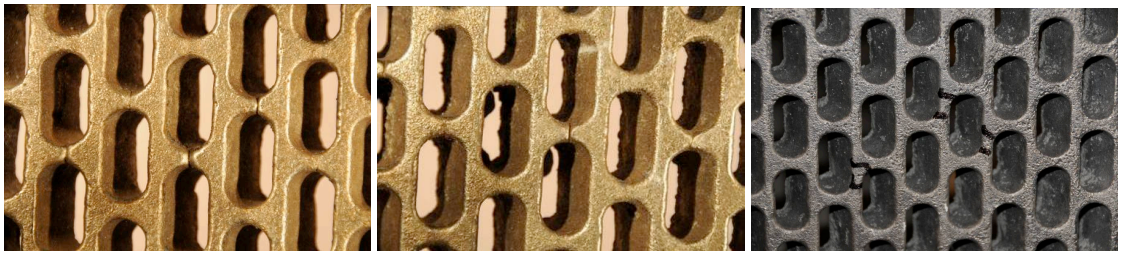

(a) (b) (c)

Figure 15. Experimental P900 castings poured at 281C° (506F°) (a), 305C° (549F°) (b), and 332Cº (598F°) (c) superheats into a 15°-tilt olivine sand mold. The plate poured with a 281C° (506F°) superheat (a) showed numerous cold shuts extending through the casting, from cope to drag. The plate poured with a 305C° (549F°) superheat (b) showed fewer cold shuts than (a), and those few did not extend through the casting. The plate poured at a superheat of 332Cº (598F°) (c) showed no cold shuts.

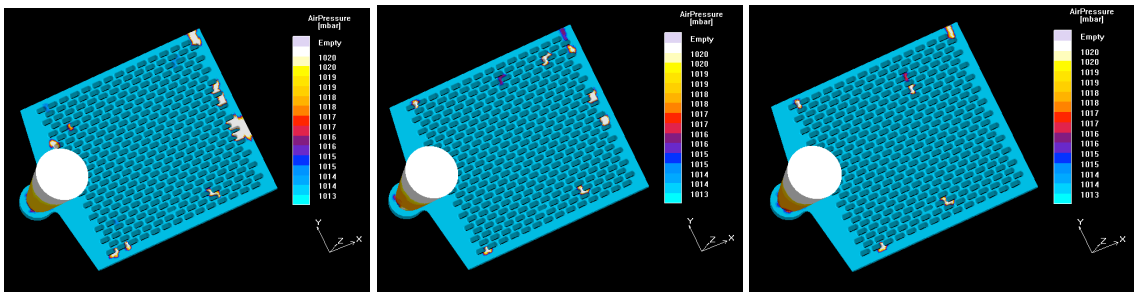

(a) (b) (c)

Figure 16. Modeler 1 air pressure simulations corresponding with the P900 plates cast with superheats of 281C° (506F°) (a), 305C° (549F°) (b), and 332Cº (598F°) (c). The higher the temperatures, the less air pressure is present in the model at 100% filled.

Energy dispersive x-ray (EDS) analysis was performed on cold shut surfaces of *Fe-Mn-Al-C* steel using a scanning electron microscope (SEM). As shown in Figure 18, the surface was partially covered by manganese and aluminum oxide films one to three microns thick.

An experimental heat was cast into a top-filled ceramic shell mold preheated to 800°C (1472°F) and poured directly from the furnace with a 180C° (324F°) superheat. This casting filled completely and had no visible casting defects (see Figure 19).

These experiments show that P900 plates can be produced defect-free from *Fe-Mn-Al-C* when adequate superheat, venting, and mold design are used. The optimal process design was simulated, and the experimental results support the simulation results.

A thermal and solidification model of a localized region of the T-junction intersections in the P900 plates was prepared and executed using Modeler 2. The Modeler 2 model provided a finely meshed localized domain to predict porosity distribution under various preheat and mold conditions. Figure 20 shows a schematic drawing of the webbed section that was modeled. Modeler 2 modeling was used to compare solidification in the horizontally bonded olivine sand mold and the vertically cast, preheated (800°C, 1472°F) ceramic shell mold. These models were then compared to T-junction sections from P900 plates cast according to the processes modeled (see Figure 21). The results indicated that the T-junctions in the horizontally cast bonded sand mold would have two areas of shrinkage porosity, and that the vertically cast ceramic shell mold T-junctions would have one central location of shrinkage porosity. P900 castings from each process were sectioned at the T-junctions and compared with the modeled results. Excellent correlation between observed casting porosity and modeling temperature predictions were found, as shown in Figure 21.

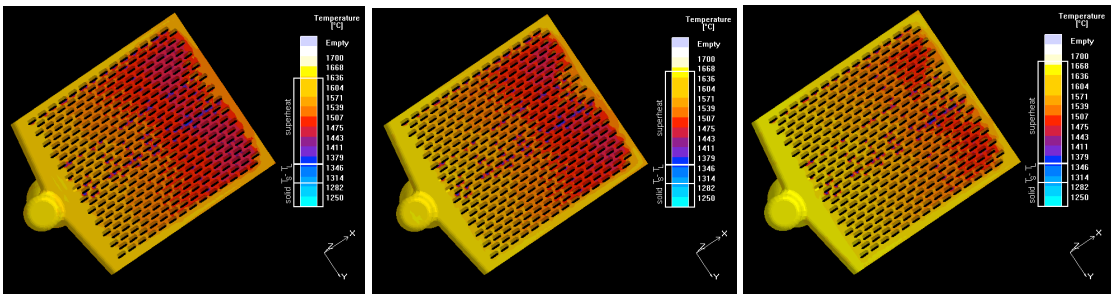

(a) (b) (c)

Figure 17. Modeler 1 temperature distribution results at 100% filled. These simulations corresponded with the P900 plates cast with superheats of 281C° (506F°) (a), 305C° (549F°) (b), and 332Cº (598F°) (c). The temperature distribution at 281C° (506F°) showed areas (in dark blue) that were near the liquidus temperature and could have produced cold shuts. These regions decreased in the simulations as superheat increased.

Filling and solidification modeling showed that the best P900 plate mold design is the vertically cast, bottom-filled, preheated ceramic shell mold. When modeled with a 300C° (540F°) superheat, this design showed no areas below the liquidus temperature in the mold at 100% filled. Air pressure results suggest that if the ceramic shell mold was vented at the top, the amount of air pressure experienced by the mold would be reduced, thus further eliminating cold

shuts. Air pressure results indicated that the preheated shell castings are less likely to form cold shut or oxide lap defects than are bonded olivine sand castings. The majority of the air pressure in the vertical preheated shell casting was at the top in the thick section, whereas the bonded olivine sand castings, especially the horizontally cast, are prone to cold shut and oxide lap formation in the thin-webbed sections. Bonded olivine sand molds can also produce successful P900 plates with the correct combination of tilt, venting, and superheat.

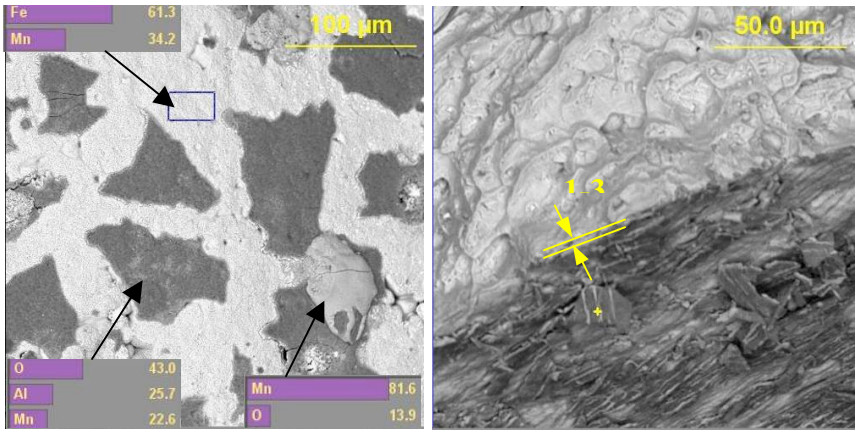

(a) (b)

Figure 18. SEM/EDS analysis of cold lap surface in *Fe-Mn-Al-C* steel.

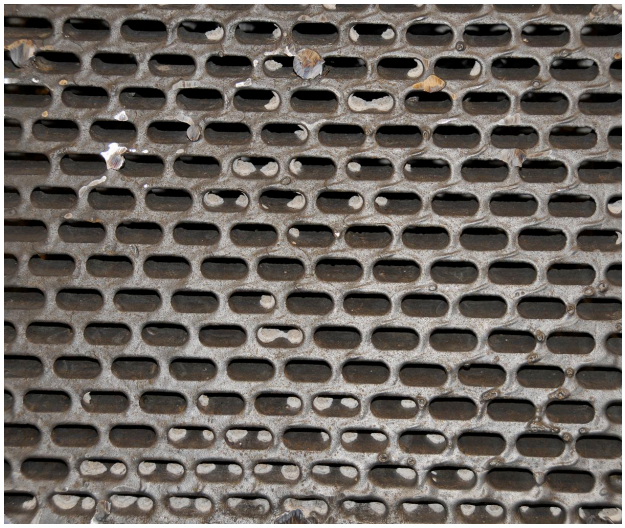

Figure 19. Section of bottom-filled P900 plate poured into a ceramic shell preheated to 800°C (1472°F) with a 180C° (324F°) superheat.

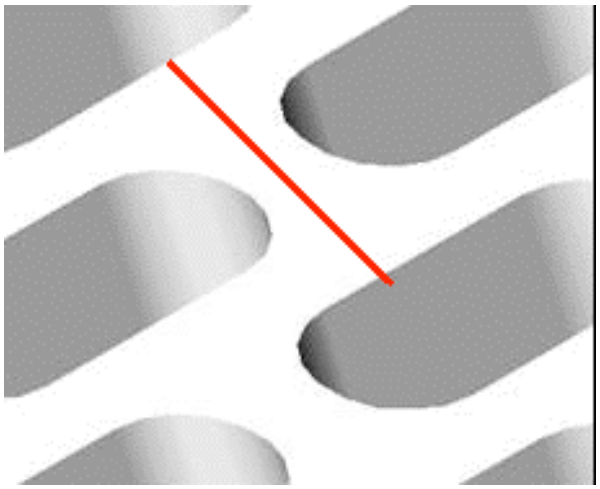

Figure 20. Web section of a P900 plate. Red line indicates where the plate was sectioned between two T- junctions for analysis.

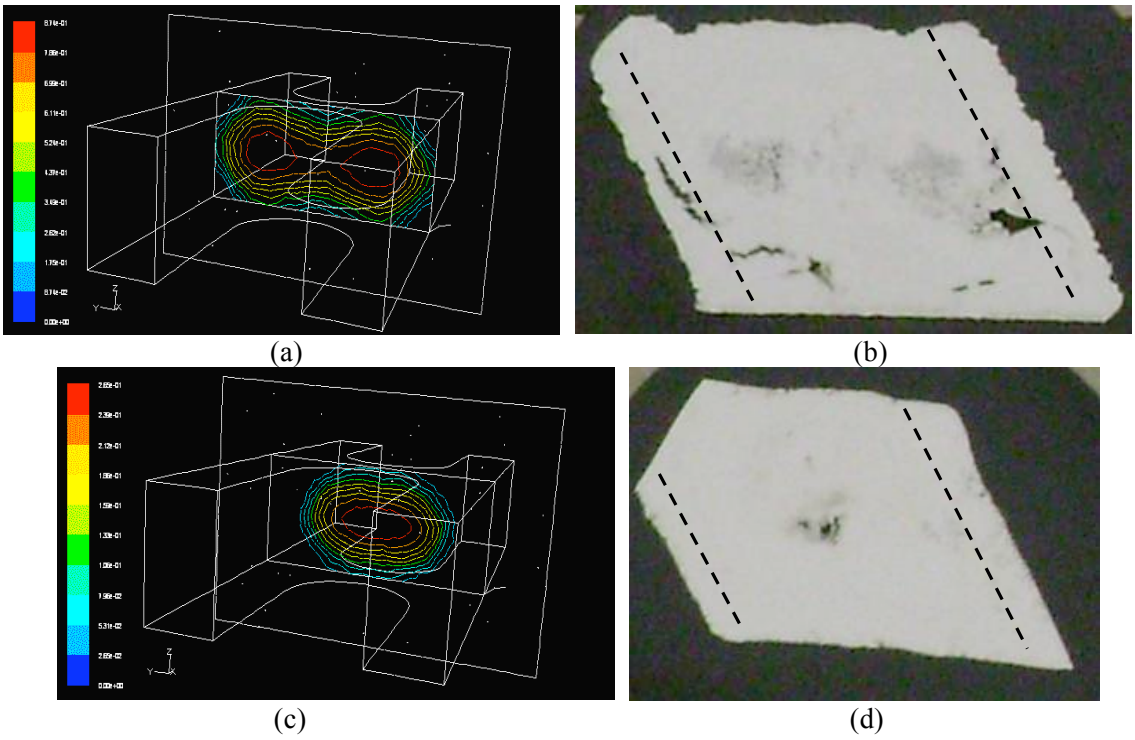

Figure 21. Modeler 2 models of T- junctions from (a) horizontally cast bonded sand P900 plate and (c) vertically cast, pre-heated (800°C, 1472°F) ceramic shell P900 plate were compared to metallographic sections through T- junctions: (b) bonded sand mold poured with 250°C (482°F) superheat and (d) ceramic shell mold poured with 180C° (324F°) superheat. Dashed lines indicate T- junctions.

CONCLUSIONS

Solidification modeling provides strong guidelines when casting lightweight, high-aluminum steel with complex mold shapes. *Fe-Mn-Al-C* parameters added to the Modeler 1 database effectively predict the location of casting defects. The horizontally cast, bonded olivine sand mold simulations showed this design to be the worst option. The multidirectional flow in the horizontally cast bonded sand mold made the prediction of the best venting procedure difficult. The P900 mold design promotes non-uniform and turbulent filling from two sides. The 15°-tilt bonded olivine sand mold design is superior to the horizontally cast bonded olivine sand mold; however, the simulations showed areas below the liquidus temperature that could create shrinkage and cold shut defects. A defect-free P900 plate was successfully cast with a superheat of 332Cº (598F°) and venting along the back (y-axis). This option may not be economical for most foundries due to the effect of high superheats on refractory life and the high oxidation rate of the *Fe-Mn-Al-C* melt. Ceramic shell molds are a much more reasonable choice when pouring complex castings from *Fe-Mn-Al-C* steel. A successful P900 plate was cast with a 180C° (324F°) superheat into a ceramic shell mold preheated to 800°C (1472°F). This casting was less porous than the bonded sand casting. It had no cold shuts or oxide film laps, and it showed no evidence of hot cracking or tearing.

FUTURE WORK

Research is continuing on investment casting of *Fe-Mn-Al-C* alloys. Future work may include more specific thermal data to permit more accurate simulations in Modeler 1. A database of *Fe-Mn-Al-C* alloys in a database in Modeler 1 would be extremely beneficial, making *Fe-Mn-Al-C* alloys more widely available to industry.

ACKNOWLEDGEMENTS

This work was supported in part by the Leonard Wood Institute under the provisions of cooperative agreement W911NF-07-2-0062 with the Army Research Laboratory.

REFERENCES

1. MIL-PRF-32269, Performance Specification, *Perforated Homogeneous Steel Armor*, (2007).

2. Howell, R.A., Montgomery, J.S., and Van Aken, D.C., "Advancements in Steel for Weight Reduction of P900 Armor Plate," *AIST Trans*. 6 (5), pp. 168-176 (2009).

3. Howell, R.A., Lekakh, S.N., Van Aken, D.C., Richards, V.L., "The Effect of Silicon Content on the Fluidity and Microstructure of Fe-Mn-Al-C Alloys," *AFS Trans.* 116, pp. 867-878 (2008).

4. Sato, K., Tagawa, K., and Inoue, Y., "Modulated Structure and Magnetic Properties of Age-Hardenable Fe-Mn-Al-C Alloys," *Met. Trans A* 21A, pp. 5-11 (1990).

5. American Foundrymen's Society, Inc., International Committee of Foundry Technical Associations, "International Atlas of Casting Defects," edited by Mervin T. Rowley, Des Plaines, Illinois, pp. 154-161 (1993).

6. American Foundry Society, "Casting Defects Handbook," pp. 105-114.

7. Campbell, J., "Castings," pp. 40, Elsevier Butterworth-Heinemann, Massachusetts (2003).

8. *Casting Defect Correlation with MAGMASOFT® Results*, MAGMASOFT® v4.4 Software Training Manual, MAGMA Foundry Technologies, Inc., Schaumburg, IL.

SECTION

2. CONCLUSIONS

Phosphorus mitigation is possible with the addition of calcium to fully react with sulfur and oxygen. This is followed by a misch metal (*Ce*) treatment to react with *P*, followed by *Ar*-stirring in the furnace to remove *Ce-P* and other inclusions. *Fe-Mn-Al-C* steel should always be melted under a protective atmosphere and poured from a ladle that offers atmospheric protection, such as a teapot or bottom-pour style ladle, if possible.

Solidification modeling software can accurately predict problem areas in complex *Fe-Mn-Al-C* castings when alloy-specific thermodynamic data is added to the database. Experimental results support the modeling results. The 15°-tilt P900 bonded olivine sand mold is superior to the horizontally cast bonded olivine sand mold, but the simulations show areas below the liquidus temperature, which could create shrinkage and cold shut defects. A defect-free P900 plate was successfully cast with a superheat of 332C° and venting along the back (y-axis). This option may not be economical for most foundries due to the effect of high superheats on refractory life and the high oxidation rate of the *Fe-Mn-Al-C* melt. Ceramic shell molds are a much more reasonable choice when pouring complex castings from *Fe-Mn-Al-C* steel. A successful P900 plate was cast with a 180C° superheat into a ceramic shell mold preheated to 800°C. This casting was less porous than bonded sand casting and had no cold shuts or oxide film laps. It also showed no evidence of hot cracking or tearing.

BIBLIOGRAPHY

[1] R.A. Howell, D.C. Van Aken, "A Literature Review of Age Hardening Fe-Mn-Al-C Alloys," *American Iron and Steel Technology*, vol. 6, no. 4 (2009).

[2] A. Prodhan, A.K. Charkrabarti, "A Study on Cast Fe-Mn-Al-Si-C Alloys," *AFS Transactions*, 37 (1990), pp. 35-46.

[3] R.A. Howell, S.N. Lekakh, D.C. Van Aken, "Quench Sensitivity of Cast Fe-30Mn-9Al-1Si-0.9C-0.5Mo Lightweight Steel," *American Iron and Steel Technology* 2 (2009), pp. 681-698.

[4] R.A. Howell, S.N. Lekakh, J.E. Medvedeva, N.I. Medvedeva, and D.C. Van Aken, "Phosphorus and Thermal Processing Effects on Charpy V-Notch Impact Toughness of Lighweight Fe-30Mn-9Al-1Si-0.9C-0.5Mo Alloy Steel," *Metallurgical and Materials Transactions A*, awaiting publication.

[5] R.A. Howell, S.N. Lekakh, D.C. Van Aken, and V.L. Richards, "The Effect of Silicon Content on the Fluidity and Microstructure of Fe-Mn-Al-C Alloys," *AFS Transactions* (2008), pp. 867-878.

[6] R.A. Howell, T. Weerasooriya, and D.C. Van Aken, "Tensile, High Strain Rate Compression and Microstructural Evaluation of Lighweight Age Hardenable Cast Fe-30Mn-9Al-XSi-0.9C-0.5Mo Steel," *AFS Transactions* (2009).

[7] W.A. Gooch, M.S. Burkins, L.F. Mills, J.W. Ogilvy, A.J. Ricchiazzi, "Cast Single Plate P900 Armor," United States Patent 5007326 (1991).

[8] "Drilling," *ASM Metals Handbook*, vol. 3, 8th edition, pp. 75-92

[9] MIL-PRF-32269, Performance Specification, *Perforated Homogeneous Steel Armor*, (2007).

[10] R.A. Howell, J.S. Montgomery, and D.C. Van Aken, "Advancements in Steel Weight Reduction of P900 Armor Plate," *Transactions of the Army Science Conference*, Orlando, Florida (2009).

[11] P.K. Panda, "Control of Moulding Raw Materials for Quality Steel Casting," *Tool and Alloy Steels,* (1990), pp. 205-213.

[12] Y. Ueda and K. Tani, "Reactions at the Interface of High Chromium Steel and Austenitic Stainless Steel with Olivine or Silica Sand Mold," *Transactions ISIJ*, 27 (1987), pp. 205-210.

[13] "No-Bake Sand Molding," *Casting*, Vol. 15, *ASM Handbook*, ASM International (2008), pp. 567-580.

[14] N. Tsujimoto, "Casting Practice of Abrasion Resistant Austenitic Manganese Steel," Presented at SEAISI 1987 Seminar in Singapore.

[15] K. Tani, Y. Ueda, and S. Mori, "Interfacial Reaction Between Cast Steel and Olivine Sand or Silica Sand," *Transactions ISIJ,* 27 (1987), pp. 197-204.

[16] J.A. Schey, "Introduction to Manufacturing Processes," second edition, McGraw Hill, Inc., 1987, pp. 166-168 (Expendable-Mold, Expendable-Pattern Casting).

[17] R.A. Horton, Investment Casting, *Casting*, Volume 15, *ASM Handbook,* ASM International, 2008, pp. 646-661.

[18] G.B. Van der Graaf, H.E.A. Van den Akker, and L. Katgerman, "A Computational and Experimental Study on Mold Filling," *Metallurgical and Materials Transactions B*, 32B (2001), pp. 69-78.

[19] S. Viswanathan and W.D. Porter, "Use of Simulation in Optimizing Mold Filling," *AFS Transactions* (2002), pp. 477-484.

[20] J. Campbell, *Castings*, 2nd edition, Oxford, UK: Elsevier (2003).

[21] D.R. Poirier and G.H. Geiger, *Transport Phenomena in Materials Processing*, Warrendale, Pennsylvania (1994).

[22] American Foundrymen's Society, Inc., International Committee of Foundry Technical Associations, "International Atlas of Casting Defects," edited by Mervin T. Rowley, Des Plaines, Illinios, (1993). Pp. 154-161.

[23] American Foundry Society, "Casting Defects Handbook," pp. 105-114.

[24] S. Kuyucak, "Solidification Temperatures and Fluidities of Nihards and High-Manganese Steels," *AFS Transactions* (2002), pp. 541-544.

[25] W.J. Jackson, "Lecture IV: Linear Surface Discontinuities," *Troubleshooting the Steel Casting Process*, ed. J.M. Svododa and B. Linskey, (1987) pp. 123-214.

[26] B.E. Brooks, C. Beckermann, and V.L. Richards, "Prediction of Burn-On and Mould Penetration in Steel Casting Using Simulation," *International Journal of Cast Metals Research*, 20 (2007), pp. 177-190.

[27] B.L. Kruse, V.L. Richards, and P.D. Jackson, "An Investigation of the Causes that Lead to Burn-in/Burn-on in Heavy Section Steel Castings," *AFS Transactions* 114 (2006), pp. 783-796.

[28] G. Krauss, "Deformation and Fracture in Maternsitic Carbon Steels Tempered at Low Temperatures," *Metallurgical and Materials Transactions A*, 32A (2001), pp. 861-877.

[29] W.M. Garrison and A.L. Wojcieszynski, "A Discussion of the Effect of Inclusion Volume Fraction on the Toughness of Steel," *Materials Science and Engineering A*, 464 (2007), pp. 321-329.

[30] W.M. Garrison and A.L. Wojcieszynski, "A Discussion of the Spacing of Inclusions in the Volume and of the Spacing of Inclusion Nucleated Voids on Fracture Surfaces of Steels," *Materials Science and Engineering A*, 505 (2009), pp. 52-61.

[31] S.H. Song, J. Wu, L.Q. Weng, and Z.X. Yuan, "Fractographic Changes Caused by Phosphorus Grain Boundary Segregation for a Low Alloy Structural Steel," *Materials Science and Engineering A*, 497 (2008), pp. 524-527.

[32] S.H. Song, H. Zhuang, J. Wu, L.Q. Weng, Z.X. Yuan, and T.H. Xi, "Dependence of Ductile-to-Brittle Transition Temperature on Phosphorus Grain Boundary Segretaion for a 2.25Cr1Mo Steel," *Materials Science and Engineering A*, 486 (2008), pp. 433-438.

[33] J.R. Cowan, H.E. Evans, R.B. Jones, and P. Bowen, "The Grain-Boundary Segregation of Phosphorus and Carbon in a Fe-P-C Alloy During Cooling," *Acta Mater.* 46 (1998), pp. 6565-6574.

[34] S. Sathyanarayanan, A. Moitra, K.G. Samuel, G. Sasikala, S.K. Ray, and V. Sigh, "Evaluation of Dynamic Fracture Toughness Based Reference Temperature of Modified 9Cr-1Mo Steel in Phosphorus Embrittled and Cold-Worked Condition," *Materials Science and Engineering A*, 488 (2008), pp. 519-528.

[35] D.M. Rodionov, M.G. Lyubinov, Y.A. Mishuntin, N.N.Stepanova, and L.V. Smirnov, "Segretation of Impurities on the Free Surface of Hadfield Steel During Heating," *Fiz. Metal. Metalloved,* 68, No. 5 (1989), pp.910-915.

[36] Y.A. Shul'te, A.A. Sherstyuk, and M.I. Kurbatov, "The Influence of Phosphorus on the Low-Temperature Embrittlement of High Manganese Steel," *Russian Castings Production,* (1963) pp. 311-313.

[37] Medvedeva, N.I., Howell, R.A., Van Aken, D.C., and Medvedeva, J.E., "Effect of Phosphorus on Brittle Fracture in κ–carbide," *Acta Materialia*, submitted for publication.

[38] C. Bangwen, Y. Dengquiang, H. Bo, and L. Li, "Application of REM in Steel," *The Minerals, Metals & Materials Society*, (1994), pp. 935-940.

VITA

Angella Marie Schulte was born September 24, 1985, in Owensville, Missouri. She attended the University of Missouri-Rolla from 2004 to 2007 and received a B.S. in Metallurgical Engineering in December 2007. During her undergraduate education she interned at Phelps Dodge Mining Company in Silver City, New Mexico, as a hydrometallurgical engineer. Upon graduation she moved on to earn an M.S. in Metallurgical Engineering from Missouri University of Science and Technology, formerly the University of Missouri-Rolla, in May 2010.